ELSEVIER

Journal of Structural Geology 28 (2006) 1569–1587

JOURNAL OF STRUCTURAL GEOLOGY

www.elsevier.com/locate/jsg

Experimental deformation of muscovite shear zones at high temperatures under hydrothermal conditions and the strength of phyllosilicate-bearing faults in nature

Elisabetta Mariani*, Katharine H. Brodie, Ernest H. Rutter

Rock Deformation Laboratory, School of Earth, Atmospheric and Environmental Sciences, University of Manchester, M13 9PL, Manchester, UK

Received 17 March 2006; received in revised form 22 June 2006; accepted 23 June 2006
Available online 21 August 2006

Abstract

Layers of fine-grained muscovite were hot-pressed then sheared between alumina sliders to shear strains up to 2, at temperatures between 300 and 700 °C, confining pressures of 206 MPa and various pore water pressures. High pore water pressures helped suppress dehydroxylation of the mica and permitted testing at temperatures higher than previously used. Shear strain rates between 10^{-3} s^{-1} and 10^{-7} s^{-1} were accessed using constant shear strain rate and stress relaxation testing. Except for strain rates $<10^{-5}$ s^{-1} at 700 °C, deformation was strain rate and temperature-insensitive, but effective normal stress-sensitive with a friction coefficient at yield of 0.3, rising with strain to 0.5. Steady-state sliding was not attained. From the mechanical data and microstructural study, deformation was inferred to have occurred by a mixture of brittle/frictional and crystal plastic processes. At 700 °C and low strain rates the shear strength falls rapidly with a linear-viscous characteristic, in a way not previously reported. This is tentatively attributed to rate-control by viscous glide of basal dislocations. Extrapolating these results to geological strain rates, we expect mica-rich fault zones will exhibit frictional behaviour with a low friction coefficient between 0.25 and 0.5, giving way at mid-crustal conditions to a rapid strength drop as viscous creep supervenes. Thus mid- to lower-crustal, mica dominated faults of any orientation, and terrains of schistose, metapelitic rocks in the cores of orogeneic belts, are expected to be very weak, supporting shear stresses in the range 1–10 MPa. The frictional behaviour of mica-rich faults in upper-crustal regions is, however, expected to be too strong to account alone for the proposed weakness of some major fault zones.

Keywords: Polycrystalline muscovite; Simulated shear zones; High temperature; Friction coefficient; Viscous glide of dislocations; Phyllosilicate-rich fault zones

1. Introduction

Geological and geophysical evidence shows that deformation in the Earth's crust is heterogeneous, with large displacements localized into faults and shear zones. As well as being an important constituent of crustal rocks, phyllosilicates are frequently observed to be the major constituents of fault rocks over a broad range of geological conditions. Clay-bearing fault gouges are commonly found in fault zones at shallow levels (Rutter et al., 1986; Zoback et al., 1987; Faulkner et al., 2003), whilst mica-rich phyllonite zones occur at deeper levels (e.g. Sibson, 1977).

Phyllosilicates can form as products of fluid-induced retrograde metamorphic reactions in fault zones down to depths of 15 km in the crust, corresponding to the greenschist facies (Wintsch et al., 1995). At still greater depths, under amphibolite facies conditions, micas may form from prograde metamorphic reactions and are often observed in high temperature mylonites (e.g. Bell and Etheridge, 1973).

In the last two decades both geological observations and experimental evidence of (1) the anomalously low frictional

* Corresponding author. Department of Earth and Ocean Sciences, University of Liverpool, L69 3GP, Liverpool, UK. Tel.: +44 151 794 5180; fax: +44 151 794 5196.
E-mail address: mariani@liv.ac.uk (E. Mariani).

0191-8141/$ - see front matter © 2006 Elsevier Ltd. All rights reserved.
doi:10.1016/j.jsg.2006.06.009

strength of some phyllosilicates (Byerlee, 1978), (2) the low differential stresses necessary to activate basal slip and kinking in mica single crystals (Etheridge et al., 1973; Kronenberg et al., 1990; Mares and Kronenberg, 1993) and (3) significant rock weakening associated with the combined effects of pressure solution and phyllosilicates (Bos and Spiers, 2002; Niemeijer and Spiers, 2005) characterized by microstructures that very closely resemble natural mylonites (e.g. Imber et al., 2001; Collettini and Holdsworth, 2004; Jefferies et al., 2006), have led to the inference that the presence of phyllosilicate minerals is one of the factors that contribute to the localization of deformation in weak zones of high shear strain.

Studies of the frictional properties of phyllosilicate-filled simulated fault zones (e.g. Shimamoto and Logan, 1981; Morrow et al., 1992; Scruggs and Tullis, 1998) confirmed the low frictional strength ($0.2 < \mu < 0.4$) of clays and micas and indicated that these minerals generally show a velocity strengthening behaviour, which is believed to inhibit stick-slip phenomena and stabilize fault motion. However, these authors pointed out that subtleties in the velocity-dependent properties of phyllosilicates should be investigated to high shear strains in order to ensure achievement of a steady stress and microstructural state. Also, the effect of temperature and pore fluid pressure should be taken into account.

Despite clays and micas being weaker than most geological materials, there are still anomalies and inconsistencies that remain to be addressed. Morrow et al. (1992) emphasized that the average shear strength of 60 MPa measured experimentally for phyllosilicate gouges is still three times higher than, for example, the average stress level of 10–20 MPa suggested for a weak San Andreas fault (Zoback et al., 1987) at corresponding depths. Furthermore, experiments at comparable fault-normal stress levels by Shea and Kronenberg (1992) showed that the yield strength measured for a polycrystalline biotite schist deformed with the main foliation at 45° to the uniaxial loading direction is significantly greater than the critical resolved shear stress of about 30–40 MPa obtained for basal slip in mica single crystals.

A key issue that faces experimentalists is the onset of dehydration reactions, which in micas deformed at nominally dry conditions begins at temperatures just above 400 °C. This sets restrictions on the possibility of trading temperature for strain rate, limiting the range of conditions that might be accessed and hence the extrapolation of experimental data to nature. Studies focussing on the intracrystalline-plastic deformation of micas were performed dry at temperatures equal to or below 400 °C in order to avoid the onset of dehydration reactions (see Shea and Kronenberg, 1992). At these conditions micas deform in the semibrittle (mean pressure-sensitive) regime over a wide range of confining pressures and support stresses that are almost insensitive to wide changes in laboratory strain rates. In earlier studies at higher temperatures (Etheridge et al., 1973; Etheridge et al., 1974), the use of high strain rates with biotite and the use of the more refractory phlogopite were the main guards against problems of dehydration.

In this paper we explore the deformation behaviour of thin layers of oriented muscovite aggregates in simulated shear zones at temperatures between 300 °C and 700 °C, at 206 MPa total confining pressure and shear strain rates as low as 7×10^{-7} s^{-1}, in constant displacement rate tests and 5×10^{-8} s^{-1} in stress relaxation tests. Controlled pore water pressures up to 103 MPa were applied to the samples and maintained throughout the experiments in order to inhibit the dehydroxylation of the muscovite aggregates, so that the higher temperature data could be extrapolated to natural strain rates with greater confidence than was possible previously.

2. Experimental methods

2.1. Characterization of the starting material

Muscovite was chosen as the starting material for three main reasons:

(1) it is one of the most common minerals in metamorphic terrains, abundant in Al-rich pelitic metasediments;
(2) upon dehydroxylation the loss of H_2O molecules leaves a residual oxygen which allows rearrangement of the crystal lattice to maintain a distorted dioctahedral configuration (Udagawa et al., 1974). This is not observed in trioctahedral micas where there is insufficient room for adjustment, hence recrystallization occurs upon dehydroxylation;
(3) dehydroxylation of muscovite does not occur homogeneously. Therefore as some OH are lost, the remaining OH become more tightly bound to the fivefold-coordinated Al cations, inhibiting or at least retarding further dehydroxylation (Guggenheim et al., 1987).

The mica powder used, wet-ground from pegmatitic muscovite, came from Hebei International Economic & Trade Developing Corporation, Hebei, China. Impurities are quartz, apatite and feldspar (<1 vol%). Its chemical formula, obtained using a Cameca SX-100 electron microprobe, is $K_{1.76}Na_{0.13}Ca_{0.02}$ $(Al_{3.36}Fe_{0.52}Mg_{0.18}Ti_{0.08})$ $(Si_{6.3}Al_{1.68})$ O_{20} $(OH)_4$. Four formula units were assumed for the hydroxyl group and normalized to oxygen. An independent determination of water content was made using thermogravimetry (TG) and differential scanning calorimetry (DSC) curves, obtained in dry argon at atmospheric pressure (Fig. 1). The weight loss observed (TG data) was interpreted to represent solely the dehydroxylation of muscovite (e.g. Guggenheim et al., 1987). This occurs in a single stage, but over a wide temperature interval. Between 640 °C and 820 °C the reaction accelerates and goes to completion (Fig. 1). The weight loss at 820 °C is 4.43 ± 0.2% of the total volume, in good agreement with the expected total hydroxyl content of muscovite. Sources of error in the determination of the total hydroxyl loss may be the presence of some interlayer water and volatilization of elements such as K^+ and Na^+. The DSC curve, obtained at a heating rate of 10 °C min^{-1}, shows a broad,

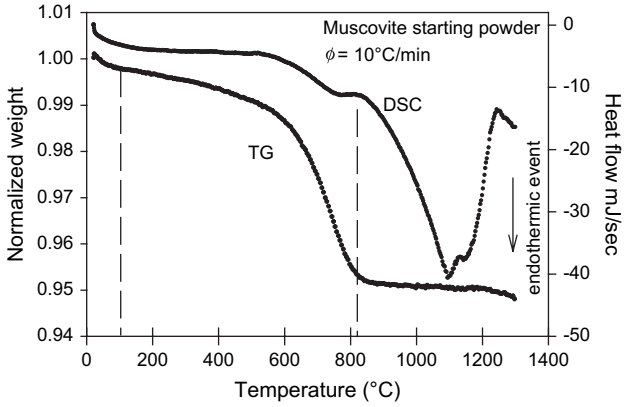

Fig. 1. TG and DSC curves obtained for the dry muscovite starting powder at a heating rate of 10 °C min^{-1}. Vertical dashed lines delineate the T interval over which structural water loss occurs in the muscovite.

slightly exothermic peak at about 600 °C and a second peak at 820 °C (Fig. 1).

The particle size distribution of the starting material was determined using a laser particle sizer (Fig. 2). Mean particle diameter is 12.7 ± 10.1 μm standard deviation. The modal particle size (the most frequently occurring observation) is 10.5 μm with median 9.1 μm (see Fig. 2). The apparent mean particle size is influenced by the marked shape anisotropy these particles display, but this result is reasonably consistent with observations made by electron microscopy.

2.2. Apparatus description

An externally heated triaxial deformation apparatus was employed, fitted with a nickel alloy (Nimonic® 115) pressure vessel that allowed deionized water to be used as the confining medium to a maximum of 700 °C at 200 MPa confining pressure. A semi-internal load cell with a resolution of ca. 0.1 MPa was used. Specimen temperature was measured using an inconel-sheathed, NiCr–NiAl thermocouple in the hollow upper loading piston (also fabricated from Nimonic® 115 alloy),

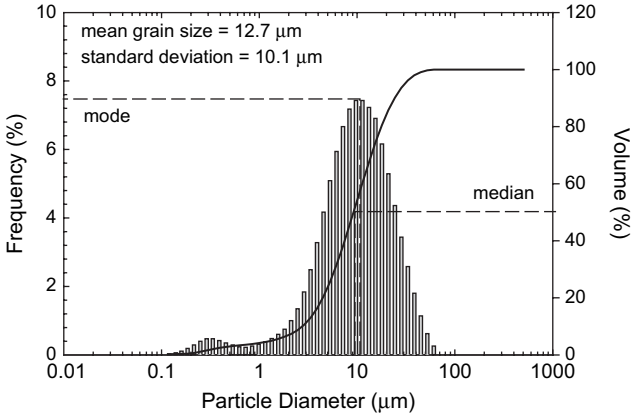

Fig. 2. Histogram of the frequency distribution and cumulative frequency distribution of the grain size of the muscovite starting powder, determined by laser particle sizer. The average grain size is 12.7 ± 10.1 μm.

through which pore water pressure was also applied to the specimen. Temperature variation along the specimen assembly (20 mm long, 9.7 mm diameter) was 3 °C at most. Sample assemblies were isolated from the confining medium by a 0.25 mm wall-thickness annealed copper jacket. Apparatus compliance was determined by loading a stiff dummy specimen at different experimental conditions.

2.3. Compaction testing procedure

Nine hot compaction experiments were performed at 206 MPa confining pressure (P_c), some with no pore water pressure (P_p) (dry, undrained), and others with P_p of 69 and 103 MPa, and in the temperature (T) range 500–700 °C. These tests, each of about 30 h duration, were designed to assess experimental conditions needed to reduce muscovite aggregates to a reasonably low porosity, the onset of dehydroxylation reactions, and their extent of progression. Experimental details are listed in Table 1.

Cylindrical muscovite aggregates for compaction tests were axially cold-pressed in their copper jackets in a die at room temperature and 206 MPa P_c. All cold-pressed samples displayed between 26.2% and 29.8% initial porosity, determined from sample density measurements compared to the theoretical density for Fe-bearing muscovite of composition comparable to ours (2.825 g cm^{-3}). Optical microscopy revealed a strong shape preferred orientation of mica platelets perpendicular to the specimen long axis and production of kinks as a result of radial shortening during cold-pressing. After the desired T, P_c and P_p were attained, the length of the jacketed specimen during time-dependent hot-pressing was measured using the 'hit point' method, in which the loading piston is used to probe for the end of the sample assembly. During pressurization and initial heating the sample length could not be monitored reliably. Specimens were hot-pressed until little further shortening occurred with time. After each compaction experiment, the specimen was carefully extracted from the copper jacket, weighed and measured to obtain density, and a small amount (≈0.016 g) ground to fine powder for TG and DSC analyses.

2.4. Preparation of muscovite-filled simulated shear zones

All specimens for deformation tests were designed to simulate a muscovite-filled shear zone where the muscovite aggregate represented the weak part of the loading column. This would undergo direct shear deformation as a 0.5 mm thick layer between rigid boundaries consisting of cylindrical recrystallized alumina forcing blocks cut at 45° to the loading (cylindrical) axis. Using thin layers of oriented flakes of muscovite between rigid forcing blocks largely obviated the problem of kinking of the mica platelets that occurred during cold compaction of cylindrical samples, and which might have a marked effect on behaviour during deformation.

The elliptical surfaces obtained along the saw-cut in the alumina cylinders were ground to a roughness of 40 μm, to

Table 1
Hot pressing and compaction experiments

Sample	P_c (MPa)	P_p (MPa)	T (°C)	ϕ_0 (%)	ϵ_v (%)	ϕ_f (%)	t (h)	Comments
wm33	206	103	700	34.5	32.6	–	49	0.57 cm, TG analysis[a]
wm34	206	103	700	34.4	34.2	–	157	0.29 cm, TG analysis[a]
wm37	206	103	700	–	–	–	276	TG analysis
wm44	206	103	700	49.6 (?)	40.5 (?)	–	504	0.86 cm, TG analysis[a]
wm51	206	–	700	26.2	12.5	14	30	TG analysis
wm52	206	–	500	27.5	10.6	18.7	30	TG analysis
wm53	206	–	600	26.6	11	16.8	30	TG analysis
wm54	206	103	600	28.3	26.1	2.8	30	TG analysis
wm55	206	103	700	26.8	27.3	0	30	TG analysis
wm56	206	103	500	27.3	23.4	5	31	TG analysis
wm57	206	69	700	27.2	26.2	0.9	31	TG analysis
wm59	206	69	600	27.1	22.8	5.3	30	TG analysis
wm60	206	69	500	26.6	19.6	8.4	30	P_p leak, TG analysis
wm110	206	103	600	–	–	–	16	Saw-cut
wm111	206	103	700	–	–	–	16	Saw-cut

List of hot pressing and compaction tests of different duration, t (in hours).
P_c is the confining pressure, P_p is the pore water pressure, T is the temperature, ϕ_0 is the initial porosity, ϵ_v is the final volumetric strain and ϕ_f is the final porosity.
[a] Copper jacket shortening.

reduce the likelihood of slippage along the sample margin during shearing. A 1 mm diameter bore was drilled through the top slider to allow direct access of pore water to the sample during a test, and filled with alumina paper to inhibit convective circulation of pore fluid in the vicinity of the specimen and loss of specimen material by extrusion or in solution. For assembly, the muscovite powder was mixed to a stiff paste with water and smeared onto the surface of the bottom slider. This induced initial shape preferred orientation of the mica flakes parallel to the slider surfaces and formed an initially 1.4 mm thick layer of muscovite powder. After drying in air at 90 °C for 30 min, the top slider was added and the assembly inserted in a previously annealed copper jacket. The contact between the bottom piston and the lower alumina slider was smeared with colloidal graphite to reduce friction and allow sideways sliding of the forcing block during a test to minimize bending of the loading column.

2.5. Experimental conditions and experiments performed

All 28 deformation experiments are listed in Table 2 and comprised:

(a) 25 constant displacement rate experiments over a range of P_c between 34 and 206 MPa, a range of P_p between ambient pressure and 103 MPa, T between 300 °C and 700 °C and at shear strain rates between 1.3×10^{-3} s^{-1} and 1.2×10^{-5} s^{-1}. These tests showed strain rate-insensitive mechanical behaviour and sensitivity of shear resistance to normal stress, thus an apparent coefficient of friction could be obtained.
(b) three long duration constant displacement rate experiments at 206 MPa P_c, 103 MPa P_p, $T = 700$ °C and at shear strain rates between 3.6×10^{-6} s^{-1} and 7×10^{-7} s^{-1}. These tests showed markedly strain rate-sensitive behaviour.
(c) 17 stress relaxation tests performed at the end of constant displacement rate tests by halting the piston advance and allowing the load to relax, at 206 MPa P_c, with P_p ranging between 34 MPa and 103 MPa and at T ranging between 400 °C and 700 °C. In these tests, shear strain rates down to 5×10^{-8} s^{-1} could be investigated over small strain increments. Experiments that employed stress relaxations are indicated in Table 2.

All direct shear (45° saw-cut) samples were pre-hot pressed for about 17 h prior to deformation at 206 MPa P_c, 103 MPa P_p and at 600 °C or 700 °C, thereby reducing the sample porosity to <3% (cf. Section 3.1). This period of hot compaction potentially allowed better equilibration of the specimen with the pore fluid, although the extent to which this occurred could not be verified.

2.6. Data processing

For constant displacement rate tests, differential load measurements were resolved into shear force along the shear direction on the saw-cut specimen, and normal force perpendicular to the shear plane which, together with the effective confining pressure (P_e) gives the normal stress. As the two forcing blocks slide, their common cross-sectional area decreases, thus the shear displacement must be taken into account to calculate resolved shear and normal stresses. Measured total axial displacements were corrected for the elastic distortion of the testing machine and used to calculate the shear strain in the sample. Also, the thickness of the sample decreases through compaction from 1.4 mm during hot-pressing at test T and P, hence the calculation of shear strain used the specimen thickness measured at the end of the test (0.5 ± 0.03 mm). In saw-cut tests the increased normal stress during deformation may reduce the shear zone thickness further by inducing some pure shear deformation. General absence of lateral

Table 2
Saw-cut experiments

Sample	P_c (MPa)	P_p (MPa)	P_e (MPa)	T (°C)	$\dot{d}$ (mm s^{-1})	τ_y (MPa)	γ_c	$\dot{\gamma}$ (s^{-1})	n	γ_r	Hot pressing (h)	Comments
wm62	206	103	103	700	4.9×10^{-5}	63	2.4	1.4×10^{-4}	9, 1.9	1.2	19	Relaxation (41)
					5.3×10^{-5}	60	1.3	1.5×10^{-4}				
wm63	206	103	103	700	1.7×10^{-4}	82	0.9	4.6×10^{-4}	1.5	1.9	17	Strain rate steps, relaxation (65)
					4.5×10^{-5}	101	1.3	1.2×10^{-4}				
wm64	206	103	103	500	5×10^{-5}	44	3.8	1.4×10^{-4}	50	0.17	16	Relaxation (15)
wm65	206	103	103	600	5.5×10^{-5}	46	3.8	1.6×10^{-4}	16	0.38	15	Relaxation (64)
wm72	206	103	103	700	4.3×10^{-6}	68	1.9	1.2×10^{-5}	6, 1	0.75	16	Relaxation (28) Jacket failure
wm73	206	103	103	600	6×10^{-6}	54	1.3	1.7×10^{-5}	16	0.21	18	Relaxation (39)
wm74	206	103	103	600	4.6×10^{-4}	53	1.7	1.4×10^{-3}	19	0.35	16	Relaxation (47) and reloading
wm75	206	103	103	500	5.2×10^{-4}	41	1.6	1.5×10^{-3}	20	0.28	16	Relaxation (44) and reloading
wm77	206	103	103	700	4.8×10^{-4}	64	2	1.4×10^{-3}	14, 1.7	1.3	16	Relaxation (121)
wm82	206	103	103	500	4.3×10^{-4}	54	2	1.3×10^{-3}			14 at 600 °C	Jacket failure
wm83	206	103	103	400	4.7×10^{-4}	49	2.5	1.4×10^{-3}			16 at 600 °C	Stick-slip
wm86	206	103	103	300	4.6×10^{-4}	40	2.8	1.3×10^{-3}			14 at 600 °C	
wm90	137	103	34	400	5.2×10^{-4}	15	3.3	1.5×10^{-3}			17 at 600 °C, 206 MPa P_c	Micro stick-slip
wm91	171	103	68	400	4.9×10^{-4}	36	2.4	1.4×10^{-3}			17 at 600 °C, 206 MPa P_c	Stick slip Jacket failure
wm92	137	103	34	500	5.2×10^{-4}	24	2.6	1.5×10^{-3}			18 at 600 °C, 206 MPa P_c	Initial stick-slip Jacket failure
wm93	171	103	68	500	5.3×10^{-4}	41	2.3	1.4×10^{-3}			17 at 600 °C, 206 MPa P_c	Initial stick-slip
wm94	137	103	34	600	5.1×10^{-4}	15	2	1.6×10^{-3}			17 at 206 MPa P_c	Initial stick-slip Jacket failure
wm95	171	103	68	600	4.8×10^{-4}	41	2.3	1.4×10^{-3}			17 at 206 MPa P_c	
wm102	206	69	137	400	5.2×10^{-4}	52	2.1	1.5×10^{-3}	26	0.19	18 at 600 °C, 103 MPa P_p	Stick-slip Relaxation (4)
wm104	206	34	172	400	4.3×10^{-4}	68	2.1	1.2×10^{-3}	49	0.24	18 at 600 °C, 103 MPa P_p	Initial stick-slip Relaxation (19)
wm106	206	34	172	400	4.4×10^{-4}	72	2.1	1.3×10^{-3}	65		17 at 700 °C, 103 MPa P_p	Stick-slip Relaxation (75)
wm107	206	34	172	700	4.5×10^{-4}	110	2	1.3×10^{-3}	19, 1.3	0.72	16 at 103 MPa P_p	Relaxation (24)
wm108	206	34	172	600	4.2×10^{-4}	98	2	1.2×10^{-3}	36	0.45	16 at 700 °C, 103 MPa P_p	Relaxation (120)
	55		39		6.1×10^{-4}	38	0.41	1.8×10^{-3}				Stick-slip. Softening
	92		76		4×10^{-4}	56	0.39	1.4×10^{-3}				Stick-slip
wm109	130	16	114	600	4×10^{-4}	79	0.23	1.4×10^{-3}			19 at 206 MPa P_c	Low hardening rate
	168		152		3.8×10^{-4}	101	0.45	1.2×10^{-3}			103 MPa P_p	Moderate hardening rate
	206		190		3.3×10^{-4}	134	0.6	9.5×10^{-4}				High hardening rate
wm115	206	34	172	500	4.9×10^{-4}	93	2.1	1.4×10^{-3}	44	0.36	18 at 700 °C 103 MPa P_p	Initial stick-slip Relaxation (161) Softening
wm117	206	103	103	700	1.2×10^{-6}	57	2.2	3.6×10^{-6}	2	0.48	17	Relaxation (69) Jacket failure
wm118	206	103	103	700	4.8×10^{-7}	43	2.3	1.4×10^{-6}	1.07	0.066	16	Moving piston seal friction effects Relaxation (24)
wm119	206	103	103	700	2.5×10^{-7}	14	2.2	7×10^{-7}			16	Moving piston seal friction effects

List of direct shear experiments on muscovite aggregates of 13 μm mean grain size, using alumina sliders for the saw-cut assembly.
P_c is the confining pressure, P_p is the pore water pressure, P_e is the effective pressure, T is the temperature, $\dot{d}$ is the axial displacement rate, τ_y is the yield shear stress, γ_c is the strain achieved with constant displacement rate tests, $\dot{\gamma}$ is the shear strain rate, n is the stress exponent in a power law and γ_r is the strain achieved with stress relaxation tests. The duration of stress relaxation tests is reported in hours in the comment column.

bulging in specimens suggests this effect is negligible for the thin specimens used here.

The shear stress calculated was corrected for the fraction of the load supported by the copper jacket.

During stress relaxation tests the stored elastic distortion of the deformation apparatus and that of the specimen translate into permanent deformation of the sample, and the deformation rate is controlled by the sample mechanical properties. Load relaxation experiments can cover a wide range of stresses and strain rates on a single specimen. Provided the results can be verified against the results of the constant displacement rate tests in which steady flow was attained, strain rates can be extended to much lower values, mainly due to the relatively small strain (1–2% axial shortening) that the sample undergoes during load relaxation. During stress relaxation tests the total displacement measured (machine plus specimen) is constant. The instantaneous permanent strain rate is proportional to the rate of force decay with respect to time, $\dot{F}$, with the constant of proportionality the combined elastic compliances of machine plus specimen (see Rutter et al., 1978; Covey-Crump, 1994). To determine $\dot{F}$, force versus time data were fitted using fifth order polynomial or exponential decay curves. The equations so obtained were then differentiated to obtain relaxation rates. This method required careful inspection of the fitted regression curves to ensure that they were adequately representative of the data set.

2.7. Electron microscopy

Microstructural analyses of the starting material and the deformed specimens were carried out using a scanning electron microscope (SEM) and a 200 kV transmission electron microscope (TEM) fitted with EDAX energy dispersive X-ray spectrometers. Mineral analyses and chemical maps were produced using a Cameca electron probe with wavelength spectrometers. The microstructure could not be resolved optically owing to the fine grain size of the muscovite aggregates. For SEM imaging, surfaces polished to 0.25 μm finish were made from longitudinally cut samples impregnated with low viscosity epoxy resin. TEM specimens were prepared by ion-thinning double-polished foils. Although this standard technique is known to introduce some damage in mica crystals, it is not generally a cause of serious problems in TEM imaging (Kogure, 2002).

3. Experimental results

3.1. Compaction experiments

All mechanical results from the compaction tests are presented graphically in Fig. 3a and 3b (see also Table 1). Little compaction occurred in samples hot-pressed under dry, undrained conditions, and the largest total volumetric strain achieved was 12.5% (corresponding to 14% final porosity). All tests performed with controlled P_p (wet) show a fast compaction rate during the first 6–12 h of testing, gradually decreasing to near constant volumes within 17 h (Fig. 3a), and

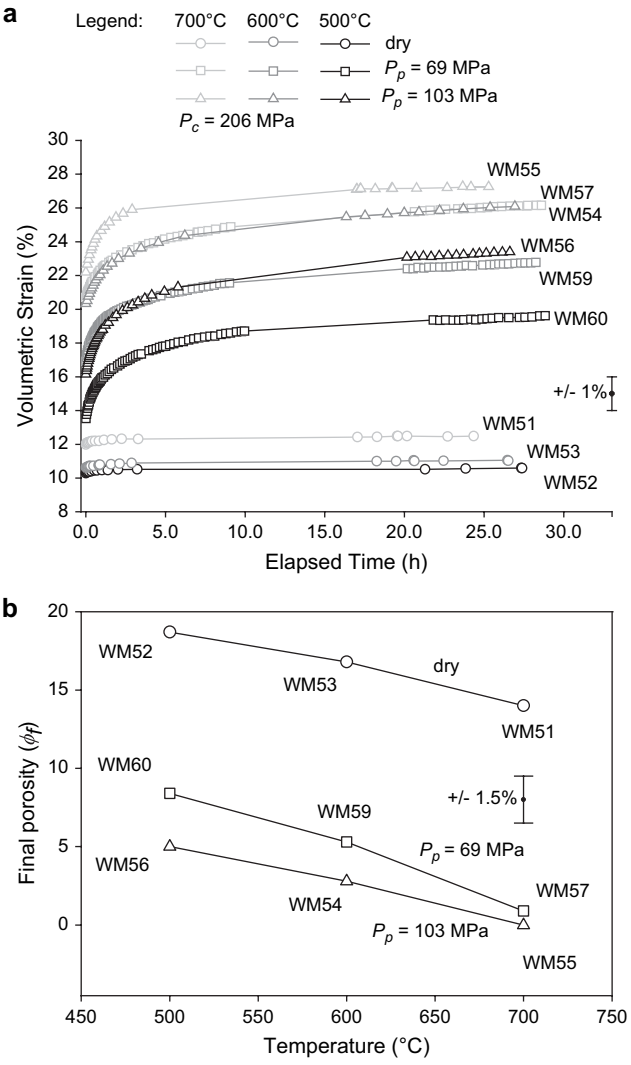

Fig. 3. (a) Volumetric strain versus elapsed time and (b) final porosity versus temperature for isostatic hot-pressing experiments. Changes in sample length were monitored with the hit-point method. Samples were tested dry (circles), at P_p of 69 MPa (squares) and 103 MPa (triangles) and T of 500 °C (black), 600 °C (dark grey) and 700 °C (light grey). All samples were tested at 206 MPa total P_c. The errors on volumetric strain and final porosity are ±1% and ±1.5%, respectively. All initial and final porosities are listed in Table 1.

with consistently larger volumetric strains at higher temperatures. Samples compacted at the same T, but different P_p, underwent larger volumetric strains at higher P_p. Thus both T and P_p enhance the compaction of muscovite aggregates. Total volumetric strains attained in wet experiments ranged up to 27%, and final porosities < 3% were obtained for samples compacted at 103 MPa P_p ($P_c = 206$ MPa) and 600 °C or 700 °C (Fig. 3b). The effects of P_p and P_e cannot be separated as the two variables were changed simultaneously.

3.2. The dehydroxylation reaction

TG analyses were performed on all the previously hot-compacted and on four hot-pressed (compaction rate not

monitored) samples. The TG curves were used to assess whether and to what extent water loss had occurred in the muscovite aggregates during hot compaction. The maximum extent of dehydroxylation during compaction occurred in specimens hot-pressed dry, at 700 °C. At these conditions the water loss attained 70% of the total water initially present (Fig. 4a). On the other hand, at 103 MPa P_p ($P_c = 200$) and 700 °C dehydroxylation during compaction was significantly reduced, with only 9% of initial water lost during 30 hour-long compaction tests (Fig. 4a) and a maximum of 12% of water lost during up to 21 day-long hot pressing tests (Fig. 4b). This shows that although dehydroxylation is enhanced by temperature, it is substantially inhibited by pore water pressure.

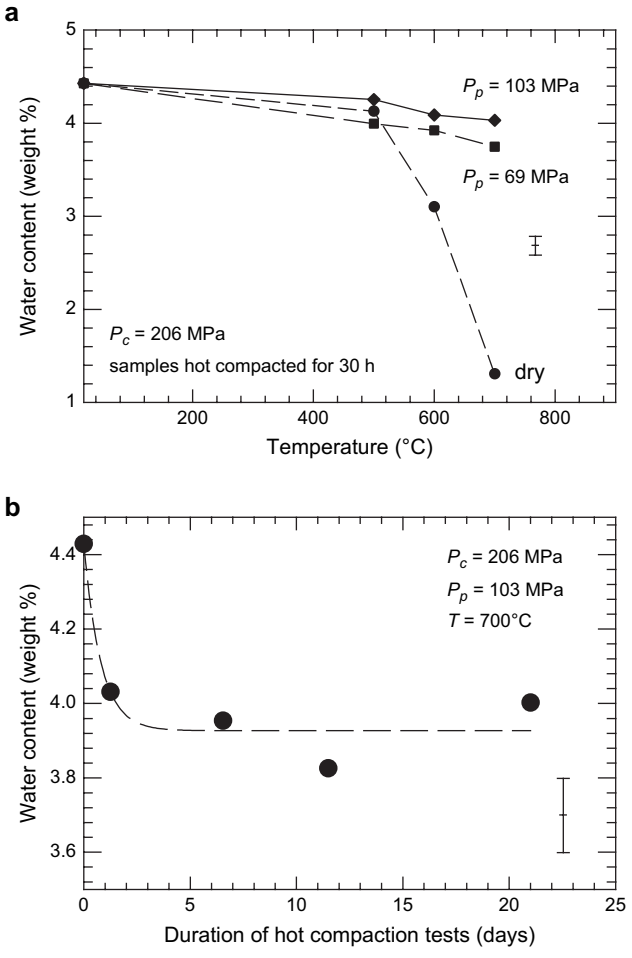

Fig. 4. TG data for previously hot-pressed muscovite aggregates. (a) showing water content (wt%) after 30 h of hot compaction at 500 °C, 600 °C and 700 °C at 206 MPa P_c, and at dry conditions, 69 MPa P_c and 103 MPa P_p. The diagram emphasizes the effect of T and P_p on the dehydroxylation reaction, and how compaction at high P_p inhibits dehydroxylation. (b) Water loss as a function of time (duration of the experiment) in samples hot pressed at 700 °C at 103 MPa P_p. After 2 days of hot compaction the water content reaches a plateau near 3.9 wt%. The water content remaining after hot isostatic compaction was calculated as the amount of water that leaves the specimen during subsequent TG. The water content of the starting material (from TG analysis) is 4.4wt%. Standard error on TG data is ±0.13 wt%.

3.3. Mechanical data from tests showing shear strain rate-insensitive behaviour

All data from these tests are presented as friction coefficient μ vs. shear strain γ diagrams (Figs. 5 and 6). This was done because in a saw-cut experiment on a material that has an intrinsic strain hardening characteristic, apparent strain hardening is exacerbated by the fact that effective resolved normal stress (σ_n) across the saw-cut increases in line with increases in resolved shear stress (τ). Also, σ_n increases as the shear contact area decreases, causing τ to increase with shear strain. By plotting the ratio τ/σ_n (rather than shear stress) versus shear strain, the non-intrinsic contributions to strain hardening can be removed.

The form of the friction coefficient versus shear strain curves obtained from these samples varies according to P_e (and P_c) and shear strain rate (Fig. 5). The slope of the elastic portion is steeper at faster strain rates. At low P_e (34 MPa) the yield point is sometimes followed by a drop in the friction coefficient in the order of 0.025 at $\gamma = 0.2$, although sample wm94 seems to be anomalously weak. At intermediate P_e (68 MPa) the yield is sharply defined, while more gradual yielding is observed at high P_e (103 MPa) (Fig. 5a, b and c). The shear strain rate has a similar effect, resulting in a well-defined yield region at fast strain rates, and a significantly wider yield portion at slower strain rates (Fig. 5e, see also Fig. 7a for comparison).

The post-yield portion of the friction coefficient–shear strain curves typically showed strain hardening (Figs. 5 and 6). Whilst this may be partly due to a faster strain rate resulting from thinning of the sample during an experiment, these curves show that the material itself does have a fairly linear intrinsic strain hardening characteristic, with apparent friction coefficient $\mu = \tau/\sigma_n$ increasing with strain and steady-state sliding not being achieved in the shear strain range of these experiments.

Although apparent work hardening caused by bending of the axial column at high strains was minimized through the use of colloidal graphite at the bottom surface of the lower forcing block, some experiments were performed with unloading after every 2% of axial shortening to allow any bending forces to be relieved before reloading (Fig. 5d). These further confirmed that strain hardening is a material characteristic. Fig. 5 also shows that the μ is largely independent of T and P_e (at a given σ_n).

Owing to the mechanical limitations of the deformation apparatus, deformation behaviour could not be tested at P_e higher than 103 MPa whilst maintaining P_p at 103 MPa. Effects of higher P_e were therefore investigated by means of confining pressure stepping experiments in which P_p was held at 16 MPa. Samples were left to stabilize at zero load at each new value of P_c for about 1 h prior to renewed deformation, to allow dissipation of any high pore pressures locally generated through increased compaction. Sample wm109 was pre-hot pressed at 600 °C and deformed at 16 MPa P_p, 600 °C and 1.4×10^{-3} s^{-1} shear strain rate. Five P_c steps were carried out, at 55 MPa, 92 MPa, 130 MPa, 168 MPa and 206 MPa

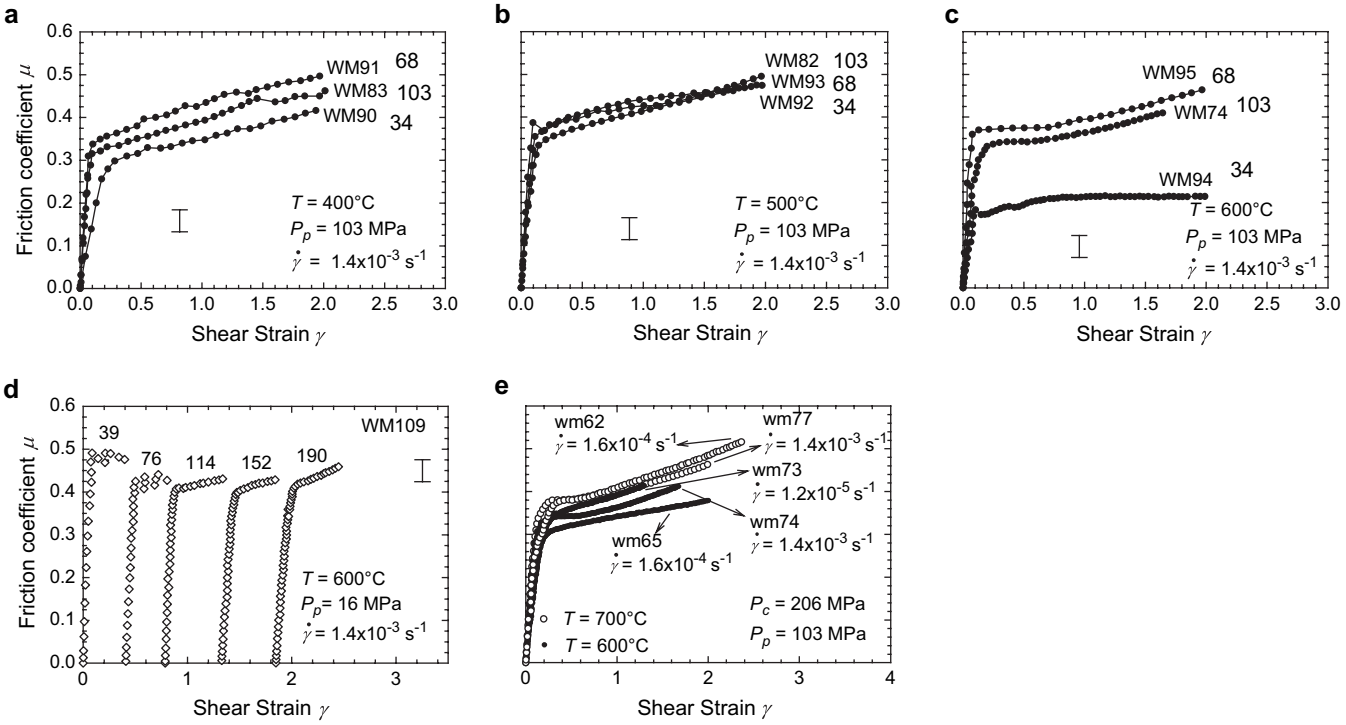

Fig. 5. Examples of data plotted as instantaneous coefficient of friction versus shear strain so that only the true strain hardening rate is apparent. (a), (b) and (c) show how behaviour is insensitive to temperature in the range 400–600 °C at a constant shear strain rate, and each graph shows curves at different P_e (indicated beside each curve in MPa) that demonstrate a relative insensitivity of μ to P_e, except for the anomalous behaviour of wm94 in (c). (d) Results of confining pressure stepping experiment wm109 at 600 °C with 16 MPa P_p. P_e (MPa) for each step are indicated. Each pressure step shows true strain hardening. (e) Shows lack of systematic sensitivity of flow behaviour to 2 decades variation in strain rate at 600 °C and 700 °C.

(shown in Fig. 5d as μ versus shear strain). The constant displacement rate curves at 39 and 76 MPa P_e were characterized by stick-slip. The true rate of strain hardening increased slightly with each step (increasing shear strain and P_e). The coefficient of friction μ decreased at first from 0.5 towards 0.4, then increased again with shear strain towards 0.5.

Fig. 5e shows the variation in effective friction coefficient over two orders of magnitude in strain rate at 206 MPa P_c, 103 MPa P_p and 600 °C and 700 °C. Within experimental uncertainty there is no apparent sensitivity of strength to strain rate.

3.3.1. The effect of temperature on mechanical behaviour

There was no decrease of μ (or the yield strength) with increasing temperature over the strain rate range 1.3×10^{-3} s^{-1} to 1.2×10^{-5} s^{-1} (Figs. 5 and 6). A first set of three experiments was performed on samples hot pressed at their subsequent deformation temperatures and deformed at 206 MPa total P_c, 103 MPa P_p, T of 500 °C, 600 °C and 700 °C and 1.4×10^{-3} s^{-1} shear strain rate. The friction coefficient increased slightly over this temperature range, on the order of 0.04 (Fig. 6a).

To test whether this behaviour was due to a real hardening effect of temperature or greater compaction of residual porosity at higher temperatures, a second set of four tests was carried out on specimens all hot pressed at 600 °C and subsequently deformed at temperatures of 300 °C, 400 °C, 500 °C and 600 °C (Fig. 6b). In the range 400–600 °C, μ was insensitive to temperature (see also Fig. 6a, b and c). Except for sample wm86 (300 °C) that yielded at a lower μ of 0.28, yield values of μ were measured at 0.33 ± 0.01, corresponding to yield shear stresses of 50 ± 4 MPa.

Experiments at higher P_e (lower P_p) were performed to assess the effect that this may have on the temperature sensitivity of the friction coefficient. Tests were carried out on samples all hot pressed at 700 °C and deformed at 34 MPa P_p and T of 400 °C, 500 °C, 600 °C and 700 °C (Fig. 6c). Friction coefficients at yield were measured at 0.3, 0.34, 0.36 and 0.39, respectively. Thus in this case a true hardening effect of temperature was observed.

The overall sensitivity of μ at yield to temperature is summarized in Fig. 6d. Depending on the effective pressure conditions, μ varies from temperature insensitive to displaying a slight hardening tendency with increasing temperature.

3.4. Mechanical data from tests showing shear strain rate-sensitive behaviour

The shear stress–shear strain curves from the slow strain rate experiments ($<1 \times 10^{-5}$ s^{-1}) at 700 °C show a low elastic limit and a broad yield region curving gently into quasi-steady state. In sample wm117 slight strain softening was observed, while wm118 and 119 showed very slight strain hardening (Fig. 7a).

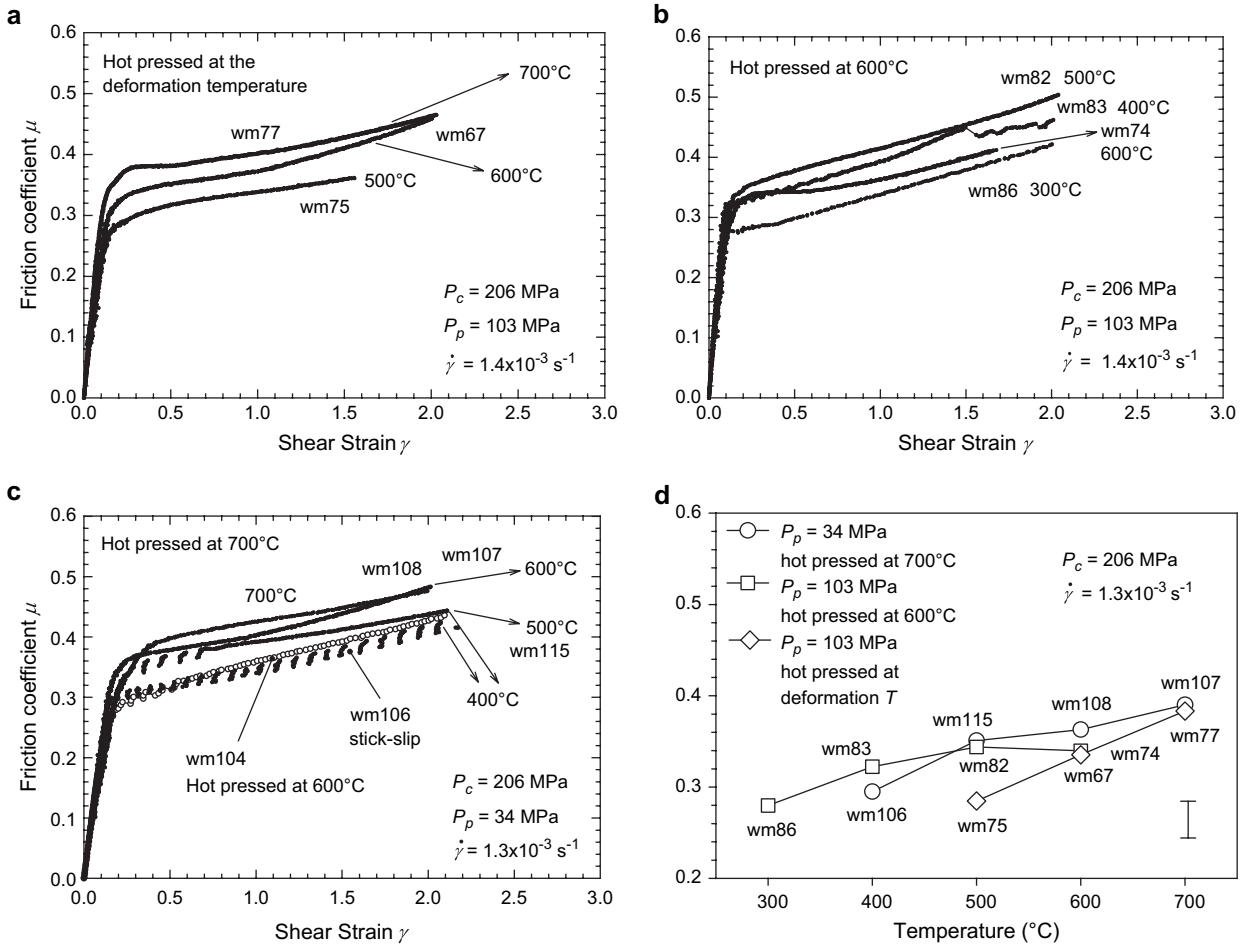

Fig. 6. (a) Friction coefficient versus shear strain diagrams from direct shear experiments at temperatures of 500, 600 and 700 °C. Specimens were pre-compacted at the deformation temperature. All tests were carried out at 206 MPa P_c, 103 MPa P_p and 1.4×10^{-3} s^{-1} shear strain rate. The curves illustrate the intrinsic strain hardening of the material. (b) Tests in the temperature range 300–600 °C on samples all hot pressed at 600 °C and deformed at 206 MPa P_c, 103 MPa P_p and 1.4×10^{-3} s^{-1} shear strain rate. (c) Tests at temperatures in the range 400–700 °C on specimens hot pressed at 700 °C, and deformed at 172 MPa P_e, 34 MPa P_p and 1.4×10^{-3} s^{-1} strain rate, apart from wm104, hot pressed at 600 °C, reported for comparison. 400 and 500 °C samples displayed stick-slip. (d) μ at yield versus T diagram that summarizes all mechanical results aimed to investigate the temperature sensitivity of shear strength. An uncertainty on μ of ±0.02, taking into account the variability between tests, is indicated.

During the slowest constant displacement rate experiments (1.4×10^{-6} s^{-1} for wm118 and 7×10^{-7} s^{-1} for wm119, with a duration of several weeks) stick-slip due to friction at the moving piston seal was observed, characterized by cycles of sudden load increments followed by a short load relaxation, at intervals of several hours. We would argue that this did not affect the mechanical behaviour of the simulated muscovite shear zones and meaningful values of shear stress and shear strain can be averaged from curves wm118 and wm119 (Fig. 7a).

The post-yield shear stresses measured for samples wm 117, 118 and 119, deformed at 3.6×10^{-6}, 1.4×10^{-6} and 7×10^{-7} s^{-1} shear strain rates, were 57, 38 and 14 MPa respectively. We presume that the flow may be described using a power law which can be written in the logarithmic form as

$$\log\dot{\gamma} = \log A + n\log\tau - Q/(2.303RT) \quad (1)$$

where $\dot{\gamma}$ is the shear strain rate (s^{-1}), A and n are material parameters, τ is the shear stress (MPa), R is the gas constant (8.3145 J mol^{-1} K^{-1}), T is the temperature (K) and Q is the activation enthalpy for flow (J mol^{-1}). Compressional strain rate $\dot{\epsilon}$, corresponding to a uniaxial shortening test, may be obtained from Eq. (1) bearing in mind that $\dot{\epsilon} = 3^{-1/2}\dot{\gamma}$. The value of the stress exponent n at 700 °C (Figs. 7b and 8b) was obtained as $n = 1.13 \pm 0.12$, indicating linear-viscous behaviour at these conditions. The transition from sharp yield in the high strain rate/low temperature stress–strain curves to a more diffuse yield at low strain rates at 700 °C is also consistent with a transition to greater stress sensitivity to strain rate.

From the present experimental data we cannot obtain a well-constrained value for Q. However, by noting that the 600 °C stress relaxation data at low strain rates do not show any transition to linear-viscous flow, we can calculate a minimum value of 270 kJ mol^{-1} for Q, and hence a value of 7.23 for log A in Eq. (1). Whilst this Q value is comparable in magnitude with previously determined activation energies for other silicate minerals (Carter and Tsenn, 1987), it is significantly higher than those obtained by Shea and Kronenberg (1992)

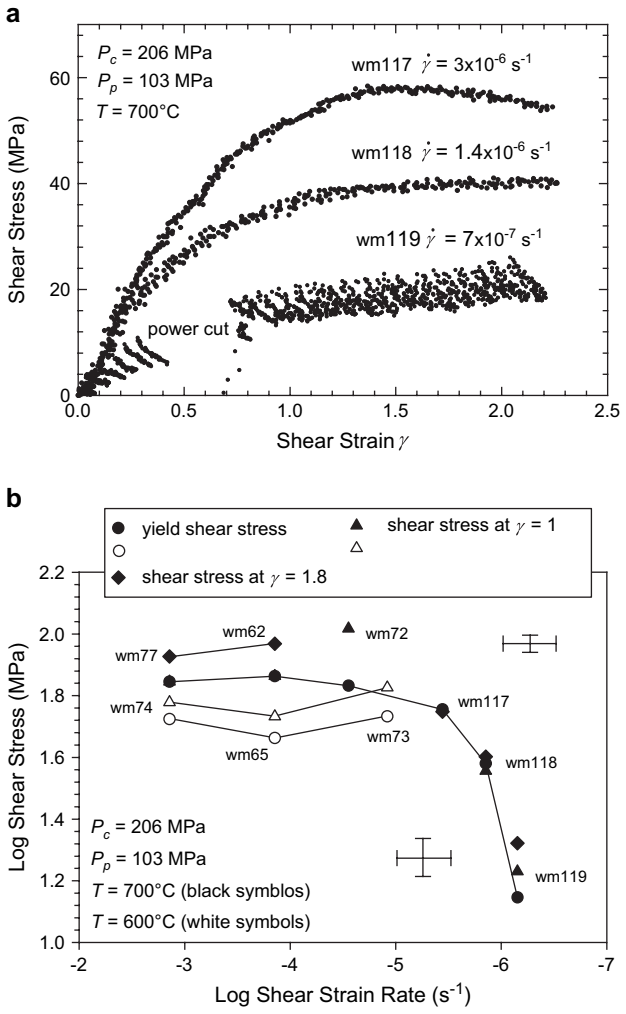

Fig. 7. (a) Shear stress versus shear strain diagram showing mechanical results obtained from direct shear experiments performed at 700 °C at shear strain rates between 3×10^{-6} s^{-1} and 7×10^{-7} s^{-1} at 206 MPa P_c and 103 MPa P_p. The apparent scatter at the lowest strain rate is due to a succession of stick slip events on the loading piston where it passes through the moving pressure seal. A power cut occurred whilst performing experiment wm119, the longest test carried out (38 days). When the power was restored the test was restarted after reestablishing the desired experimental conditions. (b) Log shear stress versus log shear strain rate graph summarizing the observed contrast between the mechanical behaviour at high shear strain rates and low shear strain rates in constant displacement rate experiments. At strain rates between 1.4×10^{-3} s^{-1} and 1.2×10^{-5} s^{-1} all samples show shear strain rate-insensitive behaviour, while in specimens deformed at shear strain rates between 3×10^{-6} s^{-1} and 7×10^{-7} s^{-1} and at 700 °C the shear stress drops dramatically as a function of strain rate. Total shear stresses supported at the yield point (circles), $\gamma = 1$ (squares) and $\gamma = 1.8$ (diamonds) are reported. All tests were at 103 MPa P_e and 600 °C or 700 °C. An error of ±5 MPa, corresponding to the error in the repeatability between tests, is reported.

for a biotite schist and Mares and Kronenberg (1993) and Kronenberg et al. (1990) for muscovite and biotite single crystals.

3.5. Stress relaxation tests

The form of stress relaxation curves obtained from low shear strain rate experiments carried out at 700 °C is markedly different from those performed at combinations of higher shear strain rate and/or lower temperatures, thus the relative mechanical results are shown separately in Fig. 8a and b. In Fig. 8b data are presented graphically as log shear stress versus log shear strain rate for comparison with previous work (e.g. Rutter and Maddock, 1992). The different locations of relaxation curves along the shear stress axis results from the different characteristics of yield and strain hardening in different specimens prior to the start of load relaxation tests.

At 400 °C, 500 °C and 600 °C, under all conditions tested (Fig. 8a), only limited decrease of the stress (approximately 6 MPa per decade reduction in shear strain rate) was observed, even at low strain rates. This behaviour is consistent with data from constant displacement rate experiments, also shown in Fig. 8a (open circles), which show no systematic stress sensitivity to the strain rate.

At 700 °C relaxation curves from samples wm62, 72, 77 and 107 at high shear strain rates show only a small stress reduction with decreasing shear strain rate, as in lower temperature tests. At shear strain rates slower than ca. 1×10^{-5} s^{-1}, however, the stress falls rapidly and the slopes of all relaxation curves approach an n value of 1 (Fig. 8b). This is consistent with the behaviour observed in constant shear strain rate tests (also shown in Fig. 8b as large open circles with best-fit line). The shear strain rate at which the stress relaxation curves begin to show rapid weakening is variable between specimens because the stress relaxation curves start after differing amounts of previous strain hardening, but it averages about 1×10^{-5} s^{-1}. Fig. 7b summarizes the generalized contrast between high shear strain rate and low shear strain rate behaviour in constant displacement rate tests.

3.6. Microstructures and chemical changes

Microstructural consequences of dehydroxylation/recrystallization reactions were investigated microstructurally in both hot compacted (for up to 21 days) and deformed (for up to 38 days) samples, in the range 500–700 °C. Representative samples were examined using mineral analysis (WDS and EDS), and scanning and transmission electron microscopy. The composition of the muscovite from (from WDS) did not change systematically or significantly in experimentally heated samples.

Strong parallel alignment of elongate mica grains was seen in all samples except for occasional kink-bands formed in the cylindrical hot-pressed samples owing to radial compaction. Samples hot-compacted and/or deformed at lower temperatures show no obvious effects of chemical reaction but those heat-treated at 700 °C developed various reaction products. Backscattered SEM images (e.g. Fig. 9a) of polished samples treated at 700 °C show small laths with a higher backscattered coefficient (lighter areas) as well as small, more equant, darker grains. Element mapping (Fig. 9b) showed that these are biotite and alkali feldspar, respectively.

TEM confirmed that all the 700 °C samples contain a number of very fine grained (100–200 nm) new phases produced by the breakdown of muscovite. Small euhedral and square crystals of an Al- and Fe-rich spinel (hercynitic spinel)

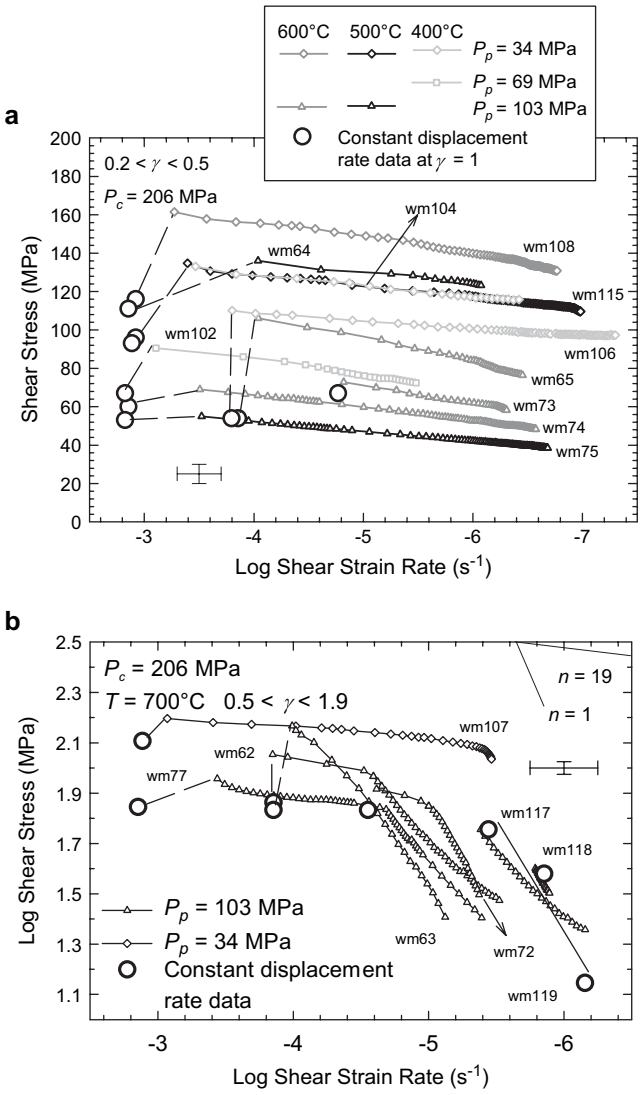

Fig. 8. (a) Shear stress versus log shear strain rate diagram representing 10 stress relaxations performed in the P_e range 103–172 MPa, at $P_c = 206$ MPa with T ranging 400 °C–600 °C. Note lack of any effect of the different experimental conditions on the shape of the relaxation curves. Constant displacement rate data (open circles) are reported for comparison. (b) Log shear stress versus log shear strain rate diagram for 7 stress relaxations at $P_e = 103$ MPa and 172 MPa, at $P_c = 206$ MPa and at 700 °C. All curves show significant slope change at strain rates $<1.4 \times 10^{-5}$ s^{-1}. Constant displacement rate data (open circles) also show a change of slope from $n = 19$ to $n = 1$. The best fit for samples wm117, 118 and 119 ($n = 1.13 \pm 0.1$) is shown. Values of n could be calculated within an uncertainty of ± 0.025. In both (a) and (b) differences in starting levels of shear stresses of the curves are related to the characteristics of strain hardening of the specimens prior to relaxation and the amount of strain at which the stress relaxation tests were commenced.

$\sim(Mg_{0.13}Fe^{2+}_{1.1})(Fe^{3+}_{0.1}, Al_{1.9})O_4$ and anhedral crystals of alkali feldspar ($K_{0.71}$ $Na_{0.12}Fe_{0.02}Mg_{0.04})(Al_{1.1}Si_{2.9}O_8$), are common (Fig. 10a and b). Needles of Al-silicate, corundum (Al-oxide) and some biotite are also present. The original muscovite contained Fe and minor Mg which explains the presence of spinel rather than Al-oxide. It is difficult to estimate the amount of reaction given the very fine grain size, although samples from long duration hot compaction (wm34, 21 days) and deformation (wm119, 33 days) tests showed more reaction than those heated for short periods. Element mapping indicated that the maximum amount of reaction products observed (e.g. wm119) is less than 10 vol% (Fig. 9b).

The very small grain size of the product crystals in our experiments made quantitative analysis of the phases difficult, even using TEM. The small amounts of Fe and Mg in the feldspar may be impurities although no lattice distortion that might be caused by such impurities was observed at the TEM scale. K_2O values were low due to volatilization under the highly focused beam, a common problem in thin film analysis. Detailed analyses of grain growth or size reduction proved difficult owing to the problem of objectively distinguishing single mica grains in SEM images. White mica also undergoes beam damage in the TEM, making investigation of dislocation structures difficult. There is no evidence of significant grain growth in any of our samples.

3.6.1. The microstructure of deformed samples

Analyses of deformed microstructures focused on comparisons between specimens that showed strain rate-insensitive behaviour and those that showed strain rate-sensitive behaviour.

3.6.1.1. Shear strain rate-insensitive behaviour. Similar microstructural features were observed in all these samples (e.g. wm64, 500 °C, wm65, 600 °C, wm106, 400 °C) despite very slow shear strain rates (8×10^{-6} s^{-1} to 5×10^{-8} s^{-1}). Individual mica grains can be seen by TEM, where they are 8–12 μm long and less than 1 μm thick (Fig. 10c). No newly crystallized reaction products were observed in these samples. The main foliation is sub-parallel to the shearing direction but is imperfect (Fig. 10c). Deformation is also heterogeneous owing to the formation of areas of intense kinking. High-angle and high amplitude kink-bands, with wavelengths on the order of 5 μm, tend to form with their axial traces at 30–40° to the foliation trace, overturned in a manner consistent with shear sense (Fig. 11a). Along kink axial traces some mica grains are fractured whilst others are folded with accompanying dilatation. R_1-oriented secondary shears (Rutter et al., 1986; Logan et al., 1992) were seen in some samples (Fig. 11b). These microstructural features imply that both crystal-plastic and brittle processes, with dilatation associated with the creation of cleavage opening and fracturing along kink axial traces, contributed to the overall deformation of these specimens.

3.6.1.2. Strain rate-sensitive behaviour. In these samples (e.g. wm62, 117, 118 and 119) the main foliation is sub-parallel to the shearing direction and little kinking was seen throughout the specimens. Porosity is very low and intergranular boundaries are difficult to distinguish in BSE images (Fig. 11c and d), in contrast to those observed in strain rate-insensitive samples, suggesting that frictional sliding was less likely along these planes during the rate-sensitive stage of the deformation. Porosity along cleavage planes is almost completely absent. All samples showed small amounts of transformation by

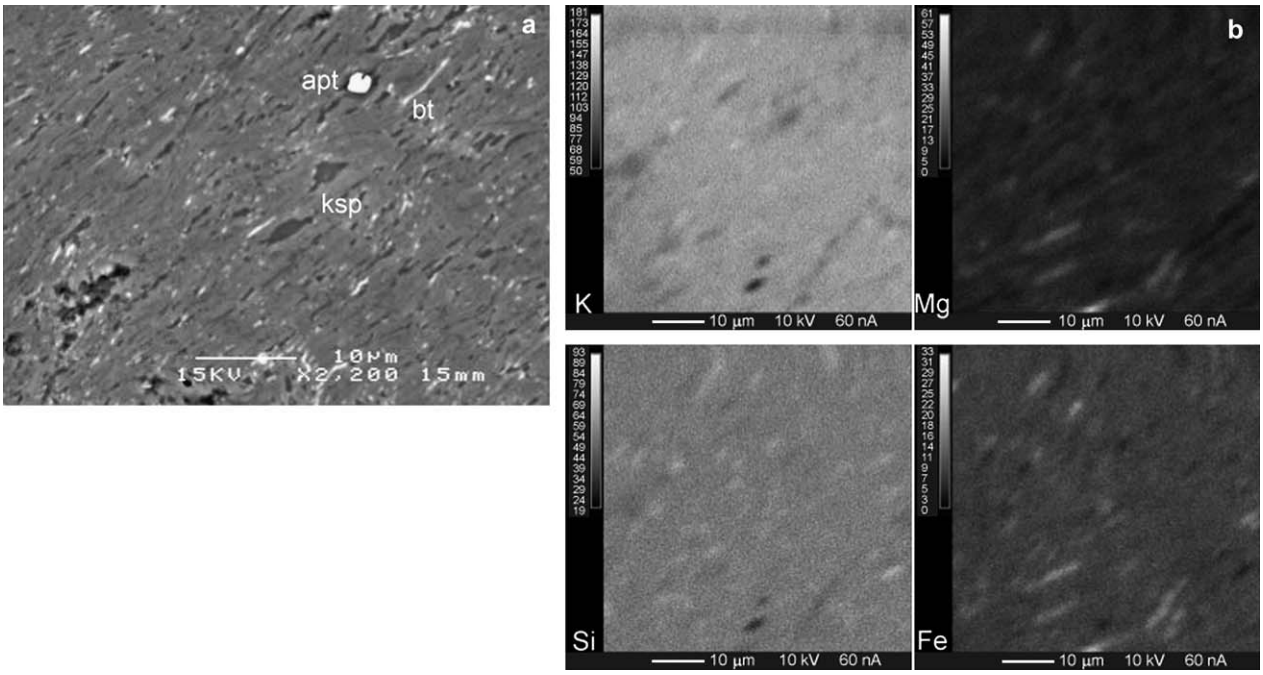

Fig. 9. (a) SEM BSE micrograph (sample wm62) showing the low porosity of samples heated at 700 °C and partial dehydration of the muscovite (that forms most of the field of view) to K-feldspar (darker areas) and biotite (bright elongate flakes). The bright phase is apatite, an impurity in the starting material. (b) Element maps for wm119 showing transformation to biotite (higher Fe and Mg, lower Si) and K-feldspar (higher Si and K) relative to the background of muscovite. The amount of transformation is estimated at less than 10 vol%.

partial dehydroxylation/breakdown of the muscovite (Figs. 9, 10a, b and d, and 11c and d). The strong alignment of biotite indicates that these grains grew following the original orientation of the muscovite flakes while the K-feldspar grains are more nearly equant. Spinel (and minor Al_2O_3 and corundum) was only seen by TEM in samples cut perpendicular to the mica foliation where it occurs as euhedral grains (Fig. 10a), implying that it forms as thin platelets parallel to the muscovite. No porosity was observed associated with the reaction products. Gentle bending of the mica grains was seen by TEM but no dislocation arrays were found in the areas investigated (Fig. 10d).

4. Discussion

4.1. Dehydroxylation and neocrystallization reactions

Muscovite dehydroxylation had previously been investigated by differential thermal analysis (DTA) (Guggenheim et al., 1987; Mazzucato et al., 1999), by *in situ* high temperature X-ray diffraction (XRD) (Guggenheim et al., 1987; Catti et al., 1989; Mazzucato et al., 1999; Muller et al., 2000) and to a lesser extent by infrared spectroscopy (Vedder and Wilkins, 1969) and electron-spin resonance (ESR) (Kalinichenko et al., 1997). In the early stages of thermal decomposition muscovite alters to a metastable dehydroxylate phase (Vedder and Wilkins, 1969; Guggenheim et al., 1987). The dehydroxylation reaction might be given as $2(OH) \rightarrow H_2O\,(\uparrow) + O_r$ where the residual oxygen (O_r) moves to the *z*-coordinate position of the Al cation. In this configuration the Al–OH bonds strengthen, inhibiting further dehydroxylation until the system thermal energy increases (Udagawa et al., 1974; see also Brigatti and Guggenheim, 2002), thereby causing dehydroxylation to be spread over the observed wide temperature range.

No data on muscovite dehydroxylation directly relevant to the experimental conditions of the present study were previously available. Our new data show that at 103 MPa P_p dehydroxylation is completely inhibited up to 500 °C. At 600 °C, the TG data and the development of minor amounts of alkali feldspar in one sample examined by TEM, suggest that the sample is undergoing incipient breakdown to a dehydroxylated phase as described by Vedder and Wilkins (1969). Specimens hot-compacted at 700 °C developed <3% new porosity and contain newly crystallized biotite and K-feldspar, although comprising no more than a few volume percent. Thus at 700 °C hydroxyl loss is also accompanied by incipient neocrystallization.

The observed reaction products are similar to those described by Brearley (1986) from a pelitic xenolith that had undergone high temperature metamorphism in a dolerite sill. Pseudomorphed muscovite grains were replaced by alkali feldspar, biotite, corundum, mullite and hercynite spinel. The reaction was incomplete and estimated to have occurred at temperatures between 900 and 750 °C over 4–5 days. The reactions he deduced were: phengite → K-feldspar + biotite + hercynite + corundum + H_2O or muscovite → K-feldspar + biotite + mullite + H_2O. The number of nuclei which form as a consequence of the muscovite breakdown is a function of the nucleation rate and the time for which nucleation had been active (Brearley, 1986). Thus in the present study,

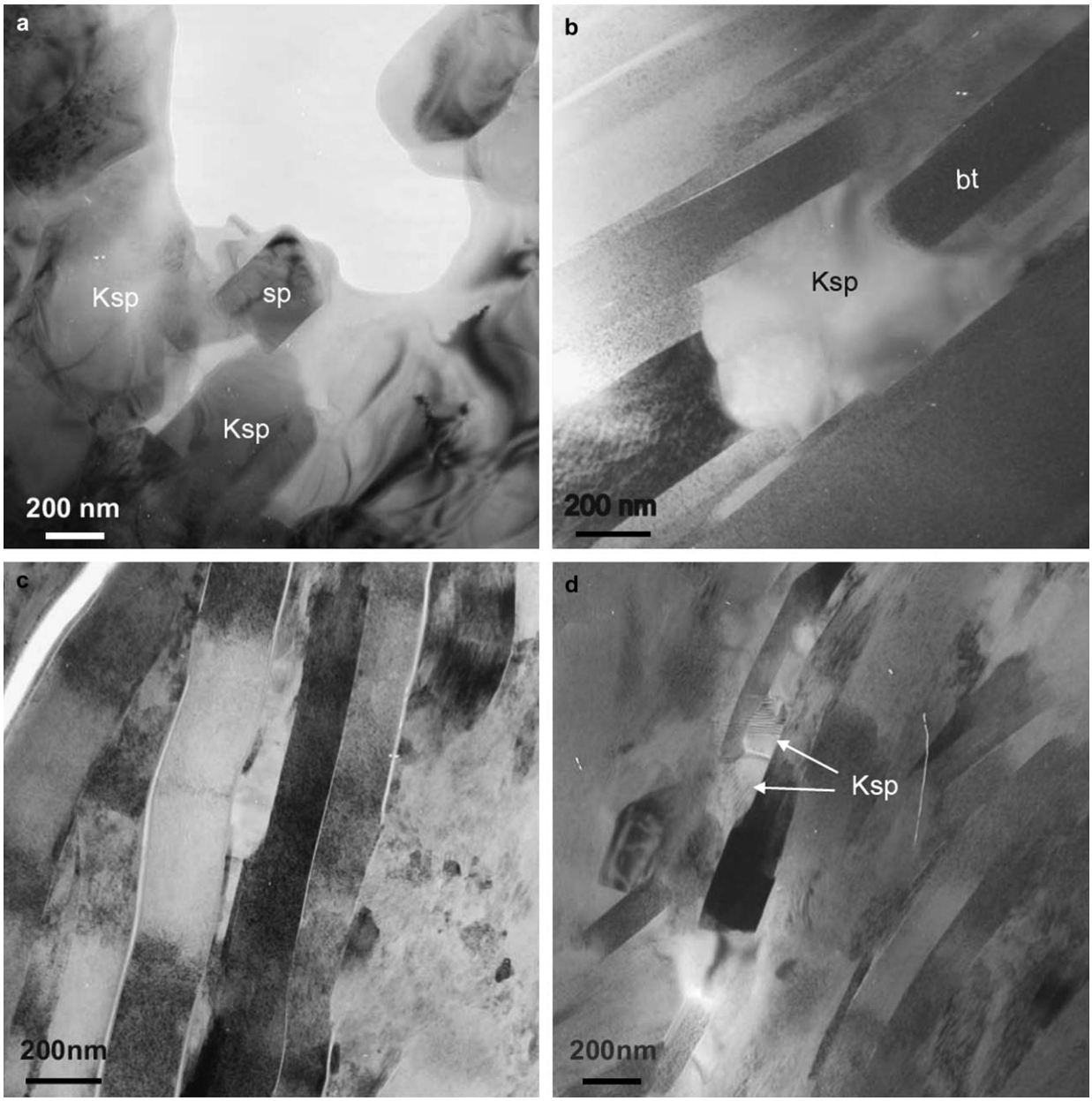

Fig. 10. Bright field TEM micrographs, (a) is oriented parallel to mica foliation, others normal to mica foliation. (a) Small newly crystallized grains of euhedral spinel (sp) and K-feldspar (Ksp), products of muscovite breakdown (sample wm117). (b) Growth of K-feldspar. The remainder of the field of view is muscovite apart from one grain of biotite (bt) (sample wm119). There is no obvious porosity preserved associated with the reaction. (c) strain rate-insensitive microstructure (wm65, 600 °C) where gentle bending of the mica flakes and minor opening of grain boundaries is apparent. Although the mica flakes are generally well-oriented, even the small misorientation is believed responsible for observed strain hardening. (d) Strain rate-sensitive microstructure (wm62, 700 °C) where the granular structure is very compact. Note local occurrence of K-feldspar (arrowed). Both samples (c) and (d) show no or very low dislocation density.

the effect of time on the progression of muscovite breakdown was investigated by performing TG on specimens hot-pressed at 103 MPa P_p and 700 °C for increasingly longer periods of time, i.e. 7, 12 and 21 days. No substantial differences in the weight loss of the three specimens was observed, suggesting that after 2 days at 700 °C the reaction slows down and then stops until the temperature is raised further (cf. Fig. 4a and b). This is substantiated by microstructural observations that showed no further increase in the amount of reaction products, even in deformed specimens (Fig. 9b). Although quantification of the amounts of reaction products was imprecise, from TG analysis a maximum of 12% of reaction products might be expected to form during isostatic hot pressing of muscovite at 700 °C, and this is consistent with SEM and TEM observations.

Deformation has been observed to enhance metamorphic reactions (Brodie and Rutter, 1985; Stünitz and Tullis, 2001). In the present study TG analysis was not performed on all deformed samples owing to the limited amount of material available and the necessity to give priority to microstructural analysis. Thus the effect of deformation on the breakdown of muscovite was studied by attempting to quantify

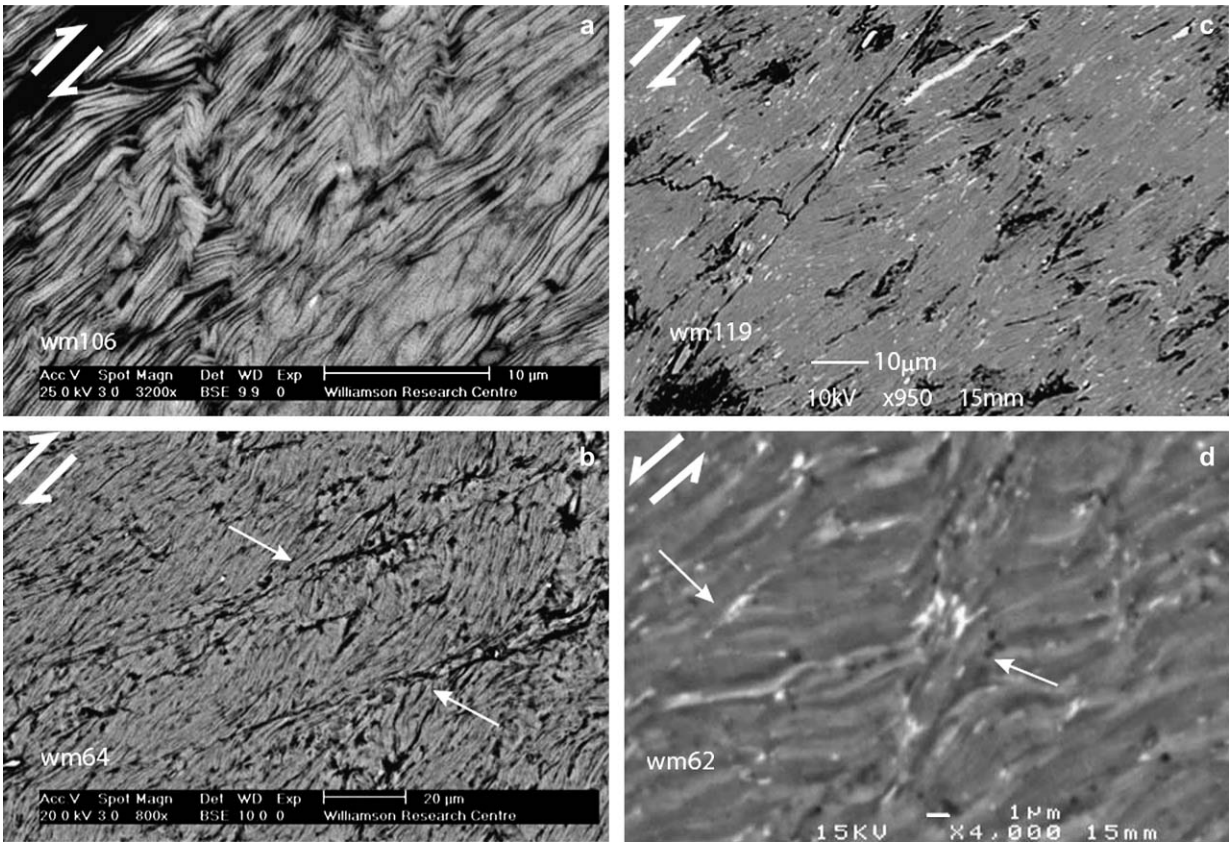

Fig. 11. BSE SEM illustrating the typical microstructures of (a and b) shear strain rate-insensitive behaviour (wm106 and 64) at 400 and 500 °C and (c and d) strain-rate sensitive behaviour at 700 °C (wm119 and 62). (a) In strain rate-insensitive samples kink-bands are commonly observed, with associated porosity, and grains boundaries are clearly seen; (b) R_1-shears are formed in parts of the samples (white arrows). (c) The muscovite grains tend to be aligned parallel to the shearing direction and reaction products of biotite and K-feldspar are observed. Grain boundaries are less distinct in SEM images. (d) Shear bands (R_1) are present in some samples (white arrows). There is no preferential development of reaction products along the shear bands. Shear sense is indicated in the top left corner of each image.

newly crystallized phases using element maps. The largest amount of reaction products (<10%) was observed in samples wm117, 118 and 119, that had been deformed, but no substantial difference in the extent to which the dehydration reaction had progressed in these three specimens was seen.

4.2. Strain rate-insensitive deformation

4.2.1. Strain hardening

In none of the shear stress versus shear strain curves obtained from constant displacement rate experiments performed in the strain rate-insensitive regime was steady-state deformation attained. Also, at these conditions the strength is effective normal stress sensitive and brittle processes and/or dilatancy-producing processes associated with inhomogeneous intracrystalline plastic deformation are implied. Strain hardening of clay-bearing fault gouges, which delays the achievement of steady-state, has often been observed in direct shear tests that do not allow large displacements (e.g. Logan and Rauenzahn, 1987; Logan et al., 1992; Rutter and Maddock, 1992).

Strain hardening effects in synthetic fault gouges have been correlated by previous authors with the evolution of the microstructure towards a steady state (e.g. Rutter et al., 1986; Logan and Rauenzahn, 1987; Logan et al., 1992). Logan and Rauenzahn (1987) observed that in clay gouges grain size reduction is not common and the development of a pattern of preferred orientation of clay platelets and superimposed shear structures are favoured processes of microstructural evolution. Logan et al. (1992) also pointed out that X, R_1 and P-oriented surfaces often develop during the strain hardening regime, their oblique orientations blocking further displacement increments and forcing deformation to spread throughout the sheared volume. Y surfaces are compatible with the simple shear imposed and hence are associated with steady state sliding. In our samples we attribute the strain hardening observed to even slight misalignments of the mica grains that then act as obstacles to sliding between grains and along the rigid boundaries of the simulated shear zone. To overcome the obstacles, higher shear stresses are required.

As kinks are also observed (cf. Section 3.6.1), dislocation glide on (001) must be active, even at low temperatures. Meike (1989) reported *in situ* TEM analysis of moving dislocations in muscovite flakes sheared at room temperature. Easy slip on only one slip system necessarily leads to kinking and dilatancy to accommodate deformation in a polycrystal. Muscovite single crystals are two to three times weaker than muscovite

aggregates and are characterized by a lower hardening rate (cf. Mares and Kronenberg, 1993). This suggests that in polycrystalline muscovite, even with a strong preferred orientation, microstructural features that are absent in single crystals, such as grain boundaries, kink-band boundaries (effectively complex dislocation walls), act as obstacles to dislocation motion and contribute to the overall work hardening observed.

Both stable and unstable sliding were observed during the strain rate-insensitive deformation, and these two different types of behaviour may be associated with specific experimental conditions. High P_p, P_e and T inhibited stick-slip in our experiments. The observation of even sporadic events of stick-slip around a mean value of friction in muscovite aggregates was surprising because phyllosilicates are generally believed to be characterized by velocity-strengthening friction behaviour (e.g. Scruggs and Tullis, 1998). Furthermore, strain hardening behaviour is expected to favour stable sliding (e.g. Logan and Rauenzahn, 1987; Rutter and Maddock, 1992). It is therefore conceivable that stick-slip could have occurred at the graphite-lubricated lower piston/lower slider interface.

4.2.2. Pressure, temperature and deformation rate sensitivity

In studies on dry micas under comparable pressure conditions but at temperatures of 400 °C or less, Mares and Kronenberg (1993), Kronenberg et al. (1990) and Shea and Kronenberg (1992) also reported μ values ranging up to 0.5, hence our results at combinations of higher strain rates and lower temperatures are comparable with the results of earlier studies. In the present study, however, the occurrence of strain hardening means we are not able to make a definitive statement about what the final, steady state friction coefficient might become.

From stress relaxation tests, shear strength seems to fall by about 6 MPa per decade of strain rate decrease (see Fig. 8a), but temperature has little systematic effect on the frictional properties over the range 400–700 °C, except for a possible slight rise in friction coefficient with increasing temperature. Moore et al. (1989) observed a similar strengthening effect of temperature for illite gouges in the range 200–600 °C. These authors measured higher total shear strengths (100–250 MPa at P_e of ca. 150 MPa) than those observed in the present study, with differences between the illite gouge strengths at different temperatures on the order of 50 MPa. This may be explained by the collapse of large volumes of residual porosity present in the specimens after the short period (1 h) of hot isostatic compaction they underwent prior to deformation. Rutter and Maddock (1992) observed similar hardening with temperature in synthetic kaolinite-quartz fault gouges, but attributed this to cementation processes associated with high temperature chemical reactions. We attribute here the observed small hardening effect of temperature to be due to a combination of progressive elimination of residual porosity coupled with sintering across basal planes of muscovite, inferred to be taking place based on the closure of grain boundaries seen in the 700 °C BSE images.

Owing to technical limitations of the deformation apparatus used it was necessary to lower the P_p to investigate behaviour at P_e higher than 103 MPa. Tests at different P_p may not be directly comparable if (a) the specimen microstructure is influenced by P_p variations or (b) as shown in Fig. 4a, at low P_p dehydroxylation of polycrystalline muscovite at high T is less inhibited. Further, when varying P_p, locally high (or low) pore pressures within the specimen may develop if permeability is particularly low (Morrow et al., 1992), with consequent effects on apparent friction. Thus values of μ obtained at 16 MPa P_p (Fig. 5d) should be considered with caution.

4.3. The shear strain rate-sensitive deformation regime

At 700 °C, rheology changes dramatically from almost strain rate-insensitive (elastic-plastic) to linear-viscous as strain rate is reduced below 1×10^{-5} s^{-1}. Linear-viscous flow has not previously been reported from experiments on mica aggregates. Linear-viscous flow is seen in materials with very small grain sizes (typically <10 μm), at slow strain rates and/or high temperatures and low stresses, when diffusion-accommodated grain boundary sliding is the dominant deformation mechanism. It is strongly grain size sensitive, with more rapid flow occurring at smaller grain sizes. Alternatively, linear-viscous behaviour may be attributed to Harper–Dorn creep, a grain size-insensitive mechanism, controlled by viscous glide of dislocations. In our experiments the change in the deformation behaviour to linear-viscous creep coincides with the onset of dehydroxylation reactions and crystallization of new phases. We must ask whether this plays a role in the mechanical behaviour observed, and whether diffusion creep or Harper–Dorn creep are active.

The transient formation of fine-grained reaction products favours a transition to grain-size sensitive flow, e.g. Rutter and Brodie (1988) for serpentinite dehydration, Stünitz and Tullis (2001) and de Ronde et al. (2004) for plagioclase-olivine aggregates, and Holyoke and Tullis (2006) for a fine-grained gneiss (Gneiss Minuti). In these cases there was sufficient transformation or connectivity of reaction products to ensure that the deformation of the new phases could control the rheological behaviour of the entire sample. In our present experiments, the small amount of transformation, albeit to very fine grain size, and its diffuse, non-interconnected development, suggests it would not be able to control the overall flow behaviour. Although the grain size of the muscovite aggregate (~13 μm) and the reaction products is small, it is still some 10-fold larger than the grain sizes required to favour grain-size sensitive flow in other experimental studies on silicates at high temperatures (e.g. Rutter and Brodie, 1988; Dimanov et al., 1999; MacDonnell et al., 1999; Stünitz and Tullis, 2001; de Ronde et al., 2004; Rutter and Brodie, 2004). We do not have experimental data over a range of grain sizes that would be required to evaluate any grain size sensitivity of the flow, but based on the above we cannot infer that the linear-viscous flow observed is controlled by grain size-sensitive, diffusion-accommodated processes. Also no microstructural evidence was observed that could be attributed to deformation by diffusive mass transfer.

Harper–Dorn creep has been reported in the low stress ($\sigma < 10^{-6}$ G in polycrystalline materials and flow stress $<10^{-4}$ G in single crystals, where G is the shear modulus), high temperature ($T \geq 0.9\,T_m$) deformation of aluminium alloys (Harper and Dorn, 1957), a few other metals, and perovskite (see Poirier, 1983). Very low dislocation densities ($\rho \approx 10^4$ cm^{-2}) are required, to minimize their long-range interactions, so that the only stress dependence comes from the glide velocity and the rheology is therefore linear. Poirier (1983) argued that Harper–Dorn creep may be an important mechanism in ceramics and in minerals such as micas, in which dislocations tend to be straight and little responsive to stress increases due to high Peierls stresses.

The linear-viscous regime in our experiments is characterized by low shear stresses for flow (~20 MPa, between 10^{-4} and 10^{-3} G) and a low dislocation density. A careful search was made by TEM for evidence of dislocation configurations, and it was clear that dislocation density was very low, on the order of one per grain. This corresponds to a maximum dislocation density of 10^6 cm^{-2}. To accommodate the observed shear strain rate (on the order of 10^{-6} s^{-1}) at this dislocation density, the average dislocation velocity must be on the order of 0.1 μm s^{-1}. We tentatively propose, therefore, that the low-stress, linear-viscous creep we observe in these mica aggregates is accommodated by viscous glide of dislocations, both within grains and at grain boundaries. We do not know whether there is any effective pressure sensitivity in this flow regime, but we anticipate that any viscous glide at grain boundaries might lead to strain incompatibilities that would lead to dilatation and some pressure sensitivity.

4.4. Geological implications of the results

4.4.1. High strain rate/low temperature, strain rate-insensitive deformation

Except at 700 °C at low strain rates, all our mechanical data resulted in shear stresses at yield between 60 MPa to a maximum of 120 MPa and a marked lack of shear strength sensitivity to temperature and strain rate. The shear strengths measured define phyllosilicates as a weak phase compared with other silicate minerals. The lack of strain rate sensitivity seems to imply that geologically meaningful inferences concerning the shear strength of crustal faults can be obtained from high strain rate laboratory experiments. This supports the widespread use in geological modelling of Byerlee's, (1978) generalization that to a first approximation the frictional strength of rocks is independent of rock type, temperature and strain rate, but is sensitive to effective pressure.

For 'hard' crustal silicates such as quartz and feldspars the friction coefficient is commonly taken to be initially about 0.85, giving way to about 0.6 at mid-crustal depths. A somewhat lower friction coefficient is often held to apply to phyllosilicate dominated fault rocks, on the order of 0.4–0.5, and more importantly without the initially high friction coefficient of 0.85 that Byerlee proposed for 'hard' rocks. Our experiments do not constrain the applicable frictional behaviour well, owing to the linear strain hardening observed up to a shear strain of 2. A steady state friction coefficient of at least 0.5–0.6 is likely to be required for the experimental conditions, but perhaps not as high as for quartzofeldspathic fault rocks. The stress relaxation experiments indicate that over sufficiently large changes in strain rate the strength of mica rocks in the brittle/dilatant-plastic regime is not entirely strain rate-insensitive. A decrease of shear strength by 6 MPa decade^{-1} of strain rate, whilst small in absolute terms, would lower shear strength at a shear strain of 2 by about 50 MPa at a strain rate of 10^{-12} s^{-1} (cf. Fig. 8a), corresponding to a friction coefficient of about 0.25 under geological conditions. Thus the strain rate sensitivity may largely compensate for the effects of strain hardening, an implication that calls for further experimental investigation.

Although friction of phyllosilicate-dominated fault rocks may be low, it does not seem to be low enough to explain the low friction coefficient (0.2) demanded of some major faults in the upper half of the continental crust, such as the San Andreas fault (e.g. Zoback et al., 1987), as a result of inferences of low *in situ* shear stress resolved along the fault zone. In this regime other factors, such as the uncontrolled variable represented by slip plane-contiguity of the mica (Wintsch et al., 1995) or possible high pore fluid pressures or processes such as pressure solution of embedded second phases in the fault gouge (e.g. Bos and Spiers, 2002; Niemeijer and Spiers, 2005) would have to be invoked.

4.4.2. Strain rate-sensitive deformation at 700 °C

The rapid weakening with decreasing strain rates observed at strain rates less than 10^{-5} s^{-1} at 700 °C implies that phyllosilicate-bearing fault zones in nature at lower temperatures may be substantially weaker than previously anticipated. In making extrapolations from our 700 °C data we must bear in mind that these experiments were carried out near the stability limits of the mica, and that we have not been able to carry out experiments at sufficiently slow shear strain rates ($<10^{-7}$ s^{-1} at 600 °C, potentially requiring experiments of several months duration) to verify the onset of rapid weakening at lower temperatures. We also do not know whether there is any pressure sensitivity of this flow, but assuming it to be dominantly due to dislocation glide we do not expect any pressure sensitivity other than that arising from the dilatancy required to accommodate strain incompatibilities between grains in which only one slip system is active.

Fig. 12 shows the predicted behaviour of mica-rich faults zones with depth, extrapolated from our 700 °C data, at three different shear strain rates, i.e. 10^{-10}, 10^{-12} and 10^{-14} s^{-1} assuming a (minimum) activation enthalpy of 270 kJ mol^{-1} and a geothermal gradient of 22 °C km^{-1}. For direct comparison with the work of Niemeijer and Spiers (2005) the geological setting of a wrench fault is considered, assuming an overburden pressure of 27 MPa km^{-1} and hydrostatic pore pressures at all depths. Behaviour at shallow depths is shown dominated by relatively rate-insensitive flow with an effective friction coefficient of about 0.5 (although it may be as low as 0.25 at geological strain rates—see above), and inferred to involve a mixture of brittle/frictional and intracrystalline plastic

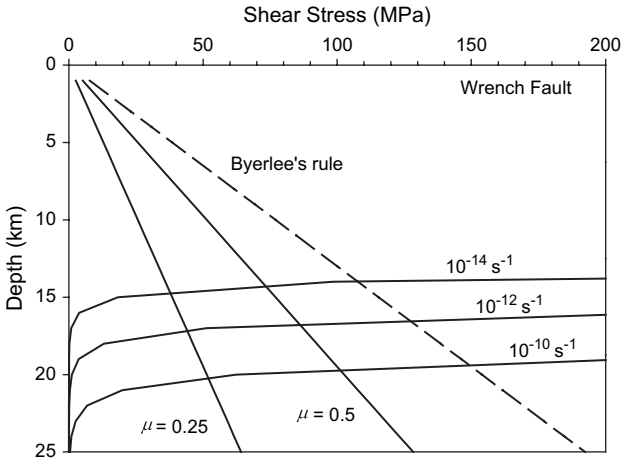

Fig. 12. Plot of depth of burial versus shear stress, to show the strength of a wrench fault according to various criteria. The geothermal gradient and the overburden pressure are assumed to be 22 °C km^{-1} and 27 MPa km^{-1} respectively. The Byerlee friction profile and friction profiles for mica-rich faults $\mu = 0.5$ and $\mu = 0.25$ as obtained from our experiments are shown. The latter two are likely to form an upper and lower bound to the behaviour of mica-rich fault zones in the upper crust. Thrust and normal fault scenarios would show higher and lower shear strengths respectively. Depth versus stress curves are shown for three different strain rates, extrapolated from our low strain rate results at 700 °C. They show dramatic strength drops at mid-crustal conditions, according to strain rate, and imply that mica-rich fault zones and metapelitic terrains under mid- to lower-crustal conditions will be very weak.

processes. The commonly assumed friction curve according to Byerlee's rule of thumb is shown for comparison ($\mu = 0.75$). For each strain rate there is a sharp transition at a particular depth to linear-viscous creep, inferred to be controlled by viscous dislocation glide. Very low shear strengths at moderate depths are predicted.

This predicted strength envelope is for a rock consisting entirely of mica with a very strong shape preferred orientation. Many phyllosilicate-bearing fault rocks have variable amounts of intermixed 'hard' phyllosilicate phases present, which will force the micaceous component to deform at a higher strain rate (and hence higher shear stress) than that externally imposed, and will also tend to impose obstructions to easy glide. Therefore these rapidly weakening strength envelopes are to be seen as lower bounds. Bos and Spiers (2002) attempted to infer the strength of quartz plus phyllosilicate rocks where pressure solution of the quartz leads to effective strengths of fault rocks substantially below the Byerlee friction line, but higher that the predictions made here for 100% mica rocks at the deeper levels. In their case the behaviour of the mica would have been in the strain rate insensitive regime. Various attempts have been made to apply the prediction of Bos and Spiers (2002) and Niemeijer and Spiers (2005) to the question of the strength of particular phyllosilicate-bearing fault zones in nature (e.g. Collettini and Holdsworth, 2004; Jefferies et al., 2006). Such attempts are based on the observation that natural microstructures in these fault zones resemble closely those obtained in the laboratory when pressure solution processes in the presence of phyllosilicates are important. This seems to suggest that these zones are weak, provided the phyllosilicates form contiguous (see Wintsch et al., 1995) and interconnected (e.g. Holyoke and Tullis, 2006) layers at the scale of the fault zone. However, if the temperatures become sufficiently high, our extrapolations show that even lower creep strengths for such faults might be expected. The strength of low angle detachment faults, which have long been a cause of controversy if 'Byerlee' frictional strength is presupposed, would no longer be an issue according to the weakness of phyllosilicate aggregates predicted from our extrapolations.

Mica-rich metapelites can be the dominant metasedimentary rock type in the cores of orogenic belts, forming thick and monotonous sequences of well foliated schists, often with little tendency to localize deformation into shear zones. The low strain rate behaviour of our samples at 700 °C implies that such schist belts are likely to form a very weak component of the crustal section during orogenesis, perhaps supporting shear stresses on the order of 1–10 MPa at an 'average' orogenic strain rate of 10^{-13} s^{-1} under upper greenschist/lower amphibolite facies conditions.

5. Conclusions

We carried out constant displacement rate and load relaxation experiments on thin layers of polycrystalline muscovite sheared wet between rigid sliders, at temperatures ranging between 400 and 700 °C. Dehydration reactions (above 400 °C) could be substantially suppressed through application of pore water pressures of ca. 100 MPa, although at 700 °C small amounts of dehydration reaction products (biotite, K-feldspar, corundum and spinel) were produced.

At shear strain rates higher than 1.4×10^{-5} s^{-1} at 700 °C and at all shear strain rates at lower temperatures, samples showed relatively strain rate-insensitive deformation behaviour. Deformation is effective normal stress-sensitive with an apparent coefficient of friction μ of about 0.3 at yield, increasing with shear strain to about 0.5 at a shear strain of 2. Strain hardening is interpreted to be due primarily to mutual misalignment of mica flakes with contributions from progressive porosity reduction and formation of oblique shear features. Shear strains sufficient to produce steady state sliding could not be attained. The friction coefficient is largely insensitive to temperature and effective confining pressure (at a given effective normal stress), but shear strength decreases slowly with decreasing strain rate at about 6 MPa decade^{-1} of strain rate.

At shear strain rates lower than 1.4×10^{-5} s^{-1} at 700 °C the shear strength falls dramatically and mechanical results indicate linear-viscous deformation, with a stress exponent (n) value close to unity. It is tentatively proposed that this may be due to viscous glide of basal dislocations in the mica becoming competitive at low strain rates, perhaps comparable to Harper–Dorn creep.

Extrapolation of the experimental data to low strain rates and pressure/temperature conditions of the continental crust suggest that the frictional strength of mica-dominated fault zones should be characterized by a friction coefficient of ca. 0.25–0.5 to mid-crustal depths depending on strain rate, and falling off rapidly to very low (1–10 MPa) shear strengths at

greater depths at the transition to linear-viscous flow. This extrapolation implies that mid-crustal, low angle detachment faults in mica-rich fault zones will be extremely weak, and that mica-dominated metapelitic terrains in mountain belts will be very weak and ductile.

Acknowledgements

This work was financed by UK NERC grant GR9/03751 and support to E.M. from the Università degli Studi di Milano, the Faculty of Science and Engineering and the School of Earth, Atmospheric and Environmental Sciences, University of Manchester, is gratefully acknowledged. We thank Rob Holloway for assistance with the use and maintenance of the deformation apparatus, Harri Williams and Steve Caldwell for technical support. E.M. thanks Julian Mecklenburgh for his encouragement and positive discussions. We would like to thank Chris Spiers and Bob Wintsch for constructive reviews.

References

Bell, T.H., Etheridge, M.A., 1973. Microstructure of mylonites and their descriptive terminology. Lithos 6, 337–348.

Bos, B., Spiers, C.J., 2002. Frictional-viscous flow of phyllosilicate-bearing fault rock: microphysical model and implications for crustal strength profiles. Journal of Geophysical Research 107, doi:10.1029/2001JB000301.

Brearley, A.J., 1986. An electron optical study of muscovite breakdown in pelitic xenoliths during pyrometamorphism. Mineralogical Magazine 50, 385–397.

Brigatti, M.F., Guggenheim, S., 2002. Mica crystal chemistry and the influence of pressure, temperature and solid solution an atomistic models. In: Mottana, A., Sassi, F.P., Thompson, J.B.J., Guggenheim, S. (Eds.), Micas: Crystal Chemistry and Metamorphic Petrology. Reviews in Mineralogy and Geochemistry 46. Mineralogical Society of America/Accademia Nazionale dei Lincei, Washington, DC/Rome, pp. 1–90.

Brodie, K.H., Rutter, E.H., 1985. On the relationship between deformation and metamorphism, with special reference to the behavior of basic rocks. In: Thompson, A.B., Rubie, D.C. (Eds.), Advances in Physics and Geochemistry. Metamorphic Reactions – Kinetics, Textures and Deformation, Vol. 4. Springer-Verlag, pp. 138–179.

Byerlee, J.D., 1978. Friction of rocks. Pure and Applied Geophysics 116, 615–626.

Carter, N.L., Tsenn, M.C., 1987. Flow properties of continental lithosphere. Tectonophysics 136, 27–63.

Catti, M., Ferraris, G., Ivaldi, G., 1989. Thermal strain analysis in the crystal structure of muscovite at 700 °C. European Journal of Mineralogy 1, 625–632.

Collettini, C., Holdsworth, R.E., 2004. Fault zone weakening and character of slip along low angle normal faults: insights from the Zuccale fault, Elba, Italy. Journal of the Geological Society of London 161, 1039–1051.

Covey-Crump, S.J., 1994. The application of Hart's state variable description of inelastic deformation to Carrara marble at $T < 450$ °C. Journal of Geophysical Research 99, 19793–19808.

de Ronde, A.A., Heilbronner, R., Stunitz, H., Tullis, J., 2004. Spatial correlation of deformation and mineral reaction in experimentally deformed plagioclase-olivine aggregates. Tectonophysics 389, 93–109.

Dimanov, A.G., Dresen, G., Xiao, X., Wirth, R., 1999. Grain boundary diffusion creep of synthetic anorthite aggregates; the effect of water. Journal of Geophysical Research 104, 10483–10497.

Etheridge, M.A., Hobbs, B.E., Paterson, M.S., 1973. Experimental deformation of single crystals of biotite. Contributions to Mineralogy and Petrology 38, 21–36.

Etheridge, M.A., Paterson, M.S., Hobbs, B.E., 1974. Experimentally produced preferred orientation in synthetic mica aggregates. Contributions to Mineralogy and Petrology 44, 275–294.

Faulkner, D.R., Lewis, A.C., Rutter, E.H., 2003. On the internal structure and mechanics of large strike-slip faults: field observations from the Carboneras fault, southeastern Spain. Tectonophysics 367, 235–251.

Guggenheim, S., Chang, Y.-H., Koster van Groos, A.F., 1987. Muscovite dehydroxylation: High-temperature studies. American Mineralogist 72, 537–550.

Harper, J., Dorn, J.E., 1957. Viscous creep of aluminium near its melting temperature. Acta Metallurgica 5, 654–665.

Holyoke III, C.W., Tullis, J., 2006. Formation and maintenance of shear zones. Geology 34 (2), 105–108.

Imber, J., Holdsworth, R.E., Butler, C.A., 2001. A reappraisal of the Sibson-Scholz fault zone model: the nature of the frictional to viscous (''brittle-ductile'') transition along a long-lived, crustal-scale fault, Outer Hebrides, Scotland. Tectonics 20, 601–624.

Jefferies, S.P., Holdsworth, R.E., Wibberley, C.A.J., Shimamoto, T., Spiers, C.J., Niemeijer, A.R., Lloyd, G.E., 2006. The nature and importance of phyllonite development in crustal-scale fault cores: an example from the Median Tectonic Line, Japan. Journal of Structural Geology 28, 220–235.

Kalinichenko, E.A., Litovchenco, A.S., Kalinichenko, A.M., Bagmut, N.N., Dekhtyaruk, N.T., 1997. The study of the kinetics and the mechanism of dhydroxylation in muscovite by ESR on Fe^{3+}. Physics and Chemistry of Minerals 24, 520–527.

Kogure, T., 2002. Investigations of micas using advanced transmission electron microscopy. In: Mottana, A., Sassi, F.P., Thompson, J.B.J., Guggenheim, S. (Eds.), Micas: Crystal Chemistry and Metamorphic Petrology. Reviews in Mineralogy and Geochemistry 46. Mineralogical Society of America/Accademia Nazionale dei Lincei, Washington, DC/Rome, pp. 281–310.

Kronenberg, A.K., Kirby, S.H., Pinkston, J., 1990. Basal slip and mechanical anisotropy of biotite. Journal of Geophysical Research 95, 19257–19278.

Logan, J.M., Dengo, C.A., Higgs, N.G., Wang, Z.Z., 1992. Fabrics of experimental fault zones: their development and relationship to mechanical behavior. In: Evans, B., Wong, T.-F. (Eds.), Fault Mechanics and Transport Properties of Rocks. Academic Press, London, pp. 33–67.

Logan, J.M., Rauenzahn, K.A., 1987. Frictional dependence of gouge mixtures of quartz and montmorillonite on velocity, composition and fabric. Tectonophysics 144, 87–108.

MacDonnell, R.D., Peach, C.J., Spiers, C.J., 1999. Flow behavior of fine grained synthetic dunite in the presence of 0.5 wt% H_2O. Journal of Geophysical Research 104, 17823–17845.

Mares, V.M., Kronenberg, A.K., 1993. Experimental deformation of muscovite. Journal of Structural Geology 15, 1061–1075.

Mazzucato, E., Artioli, G., Gualtieri, A., 1999. High temperature dehydroxylation of muscovite-$2M_1$: a kinetic study by in situ XRPD. Physics and Chemistry of Minerals 26, 375–381.

Meike, A., 1989. In-situ deformation of micas: a high voltage electron microscopy study. American Mineralogist 74, 780–796.

Moore, D.E., Summers, R., Byerlee, J.D., 1989. Sliding behaviour and deformation textures of heated illite gouge. Journal of Structural Geology 11 (3), 329–342.

Morrow, C., Radney, B., Byerlee, J., 1992. Frictional strength and the effective pressure law of montmorillonite and illite clays. In: Evans, B., Wong, T.-F. (Eds.), Fault Mechanics and Transport Properties of Rocks. Academic Press, London, pp. 69–88.

Muller, F., Drits, V.A., Plançon, A., Besson, G., 2000. Dehydroxylation of Fe^{3+}, Mg-rich dioctahedral micas: (I) structural transformation. Clay Minerals 35, 491–504.

Niemeijer, A.R., Spiers, C.J., 2005. Influence of phyllosilicates on fault strength in the brittle-ductile transition: insights from rock analogue experiments. In: Bruhn, D., Burlini, L. (Eds.), Microstructural Evolution and Physical Properties in High Strain Zones. Geological Society, London, Special Publications 245, pp. 303–327.

Poirier, J.-P., 1983. Creep of Crystals – High Temperature Deformation Processes in Metals, Ceramics and Minerals. Cambridge University Press, Cambridge.

Rutter, E.H., Atkinson, B.K., Mainprice, D.H., 1978. On the use of the stress relaxation testing method in studies of the mechanical behavior of geological materials. Geophysical Journal of the Royal Astronomical Society 55, 155–170.

Rutter, E.H., Brodie, K.H., 1988. The role of tectonic grain size reduction in the rheological stratification of the lithosphere. Geologische Rundschau 77, 295–308.

Rutter, E.H., Brodie, K.H., 2004. Grain size sensitive flow in hot-pressed, fine-grained quartzite. Journal of Structural Geology 26, 2011–2023.

Rutter, E.H., Maddock, R.H., 1992. On the mechanical properties of synthetic kaolinite/quartz fault gouge. Terra Nova 4, 489–500.

Rutter, E.H., Maddock, R.H., Hall, S.H., White, S.H., 1986. Comparative microstructures of natural and experimentally produced clay-bearing fault gouges. Pure and Applied Geophysics 124 (1/2), 3–30.

Scruggs, V.J., Tullis, T.E., 1998. Correlation between velocity dependence of friction and strain localization in large displacement experiments on feldspar, muscovite and biotite gouge. Tectonophysics 295, 15–40.

Shea, W.T., Kronenberg, A.K., 1992. Rheology and deformation mechanisms of an isotropic mica schist. Journal of Geophysical Research 97, 15201–15237.

Shimamoto, T., Logan, J.M., 1981. Effects of simulated clay gouges on the sliding behavior of Tennessee sandstone. Tectonophysics 75, 243–255.

Sibson, R.H., 1977. Fault rocks and fault mechanisms. Journal of the Geological Society of London 133, 191–213.

Stünitz, H., Tullis, J., 2001. Weakening and strain localization produced by syn-deformational reaction of plagioclase. International Journal of Earth Sciences 90, 136–148.

Udagawa, S., Urabe, K., Hasu, H., 1974. The crystal structure of muscovite dehydroxylate. Japanese Association of Mineralogy. Petrology and Economic Geology 69, 281–389.

Vedder, W., Wilkins, R.W.T., 1969. Dehydroxylation and rehydroxylation, oxidation and reduction of micas. The American Mineralogist 54, 482–509.

Wintsch, R.P., Christoffersen, R., Kronenberg, A.K., 1995. Fluid-rock reaction weakening of fault zones. Journal of Geophysical Research 100 (B7), 13021–13032.

Zoback, M.D., Zoback, M.L., Mount, V.S., 1987. New evidence on the state of stress on the San Andreas fault system. Science 238, 1105–1111.